

Accepted Manuscript

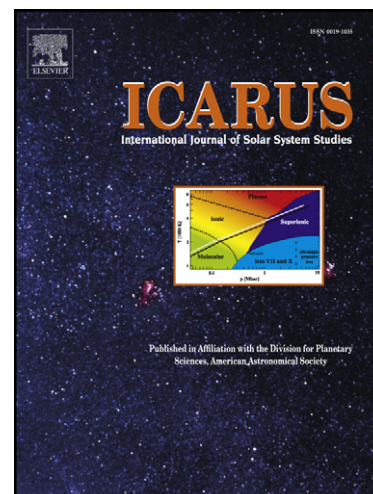
Nonuniform cratering of the Moon and a revised crater chronology of the inner solar system

Mathieu Le Feuvre, Mark A. Wieczorek

PII: S0019-1035(11)00094-7
DOI: [10.1016/j.icarus.2011.03.010](https://doi.org/10.1016/j.icarus.2011.03.010)
Reference: YICAR 9753

To appear in: *Icarus*

Received Date: 18 August 2010
Revised Date: 1 March 2011
Accepted Date: 7 March 2011



Please cite this article as: Le Feuvre, M., Wieczorek, M.A., Nonuniform cratering of the Moon and a revised crater chronology of the inner solar system, *Icarus* (2011), doi: [10.1016/j.icarus.2011.03.010](https://doi.org/10.1016/j.icarus.2011.03.010)

This is a PDF file of an unedited manuscript that has been accepted for publication. As a service to our customers we are providing this early version of the manuscript. The manuscript will undergo copyediting, typesetting, and review of the resulting proof before it is published in its final form. Please note that during the production process errors may be discovered which could affect the content, and all legal disclaimers that apply to the journal pertain.

1 Nonuniform cratering of the Moon and a
2 revised crater chronology of the inner solar
3 system.

4 Mathieu Le Feuvre* and Mark A. Wieczorek

5 *Institut de Physique du Globe de Paris, Saint Maur des Fossés, France.*

6 Copyright © 2010 Mathieu Le Feuvre

7 Number of pages: 60

8 Number of tables: 9

9 Number of figures: 9

* Now at Laboratoire de Planétologie et Géodynamique,

Université de Nantes, France.

Email address: mathieu.lefeuvre@univ-nantes.fr (Mathieu Le Feuvre).

1 **Proposed Running Head:**

2 Cratering of the Moon and inner planets

3 **Please send Editorial Correspondence to:**

4

5 Mathieu Le Feuvre

6 Laboratoire de Planétologie et Géodynamique

7 Université de Nantes

8 UMR CNRS 6112

9 2, rue de la houssinière, BP 92208

10 44322 NANTES cedex 03, France.

11 Email: mathieu.lefeuvre@univ-nantes.fr

1 ABSTRACT

2 We model the cratering of the Moon and terrestrial planets from the present
 3 knowledge of the orbital and size distribution of asteroids and comets in the
 4 inner solar system, in order to refine the crater chronology method. Impact
 5 occurrences, locations, velocities and incidence angles are calculated semi-
 6 analytically, and scaling laws are used to convert impactor sizes into crater
 7 sizes. Our approach is generalizable to other moons or planets. The lunar
 8 cratering rate varies with both latitude and longitude: with respect to the
 9 global average, it is about 25 % lower at ($\pm 65^\circ\text{N}, 90^\circ\text{E}$) and larger by the
 10 same amount at the apex of motion ($0^\circ\text{N}, 90^\circ\text{W}$) for the present Earth-Moon
 11 separation. The measured size-frequency distributions of lunar craters are rec-
 12 onciled with the observed population of near-Earth objects under the assump-
 13 tion that craters smaller than a few kilometers in diameter form in a porous
 14 megaregolith. Varying depths of this megaregolith between the mare and high-
 15 lands is a plausible partial explanation for differences in previously reported
 16 measured size-frequency distributions. We give a revised analytical relation-
 17 ship between the number of craters and the age of a lunar surface. For the
 18 inner planets, expected size-frequency crater distributions are calculated that
 19 account for differences in impact conditions, and the age of a few key geologic
 20 units is given. We estimate the Orientale and Caloris basins to be 3.73 Ga old,
 21 and the surface of Venus to be 240 Ma old. The terrestrial cratering record
 22 is consistent with the revised chronology and a constant impact rate over the
 23 last 400 Ma. Better knowledge of the orbital dynamics, crater scaling laws and
 24 megaregolith properties are needed to confidently assess the net uncertainty
 25 of the model ages that result from the combination of numerous steps, from
 26 the observation of asteroids to the formation of craters. Our model may be

1 inaccurate for periods prior to 3.5 Ga because of a different impactor popula-
2 tion, or for craters smaller than a few kilometers on Mars and Mercury, due
3 to the presence of subsurface ice and to the abundance of large secondaries,
4 respectively. Standard parameter values allow for the first time to naturally
5 reproduce both the size distribution and absolute number of lunar craters up
6 to 3.5 Ga ago, and give self-consistent estimates of the planetary cratering
7 rates relative to the Moon.

8 *Keywords:* cratering ; Moon ; terrestrial planets ; crater chronology ; impact
9 processes

1 Introduction

2 The counting of impact craters offers a simple method to estimate the ages of
 3 geologic units on planetary surfaces when in situ rock samples are lacking. The
 4 crater chronology method is based on the simple idea that old surfaces have
 5 accumulated more impact craters than more recent ones (Baldwin, 1949). The
 6 relationship between geologic age and number of lunar craters, based on the ra-
 7 diometric dating of existing lunar rock samples, is found to be approximately
 8 linear from the present to about 3 Ga ago, and approximately exponential
 9 beyond that time (Neukum et al., 2001a; Stöffler and Ryder, 2001, and refer-
 10 ences therein). For statistical robustness, craters are generally counted within
 11 a number of consecutive diameter ranges, allowing one to recognize certain
 12 biases, such as erosion, resurfacing or crater saturation processes. Measure-
 13 ments over various geologic units has led to the postulate that the relative
 14 shape of the size-frequency distributions (SFD) of lunar impact craters was
 15 similar for all surfaces, but unfortunately, the exact shape of this production
 16 function in the 2–20 km kilometer range is still debated after decades of study.
 17 The total predicted size-frequency distribution for any given time is obtained
 18 by multiplying the production function, assumed independent of age, by a
 19 time-variable constant. The age of a geologic unit is estimated by finding the
 20 best fit between the standardized and measured distributions.

21 The approach taken in this work models directly crater distributions from the
 22 current knowledge of the impactor population. This allows us to infer prop-
 23 erties of the impact history of a planetary body that the sole observation of
 24 craters could not reveal. In particular, whereas the crater chronology method
 25 assumes that craters accumulate uniformly on the surface of the planetary

body, this method allows to quantify possible spatial variations in the impact rate. Moreover, in the absence of dated samples with known geological context from Mercury, Venus and Mars, the generalization of the crater chronology to these planets requires an estimate of the relative cratering rates with respect to the Moon: in the same period of time, the number of craters of a given size that form on two planets differ according to both the different impact probabilities of the planet crossing objects and the impact conditions (e.g., impact velocity, surface gravity).

Using this bottom-up approach, Neukum et al. (2001b) proposed age estimates of mercurian geologic features based on a Mercury/Moon cratering rate ratio estimated from telescopic observations. Similarly, Hartmann and Neukum (2001) adapted the lunar cratering chronology to Mars, using the Mars/Moon cratering rate ratio of Ivanov (2001). The venusian surface, which contains a small number of craters that appear to be randomly distributed, has been the subject of several attempts of dating. The most recent estimates can be found in Korycansky and Zahnle (2005) and McKinnon et al. (1997), and are both based on the population of Venus crossers as estimated by Shoemaker et al. (1990). In this study, we use improved estimates of the orbital characteristics and size-frequency distribution of the impactor population.

The early lunar cratering record indicates that impactors were hundred of times more numerous than today, possibly due to the massive injection in the inner system of main-belt and/or Kuiper-belt objects about 700 Ma after the Moon formed, an event known as the Late Heavy Bombardment (LHB) (see Gomes et al., 2005; Tera et al., 1974; Hartmann et al., 2000). More than 3 Ga ago, the impactor population appears to have reached a relative state of equilibrium, being replenished both in size and orbit by, respectively, collisions

1 inside the main asteroid belt and the ejection by resonances with the giant
 2 planets (Bottke et al., 2002). Under the assumption of a steady state distrib-
 3 ution of impactors, the distribution of craters on ~ 3 Ga old surfaces should
 4 be consistent with the present astronomically inferred cratering rates.

5 The lunar cratering record, in the form of the standardized production func-
 6 tions, agrees reasonably well with telescopic observations of planet-crossing ob-
 7 jects down to a few kilometers in diameter (Stuart, 2003; Werner et al., 2002).
 8 Smaller craters appear to be not numerous enough to have been formed by an
 9 impacting population similar to the present one. But, in Ivanov and Hartmann
 10 (2007), it was suggested that the presence of a porous lunar megaregolith may
 11 reduce the predicted size of small craters, accounting for this observation. In
 12 Strom et al. (2005), the distinction was made between pre- and post-LHB lu-
 13 nar crater distributions. Older distributions, depleted in small craters, would
 14 reflect the SFD of Main Belt asteroids - massively provided by the LHB -
 15 rather than the SFD of Near-Earth asteroids. Marchi et al. (2009) revised the
 16 crater chronology method by deriving a new production function from impact
 17 modeling that differs significantly from those based on measurements. In this
 18 study, we attempt to fully reconcile the measured lunar production functions
 19 with the telescopic observations of planet-crossing objects.

20 Modeling the impact bombardment also allows us to quantify spatial cratering
 21 asymmetries that are not accounted for in the traditional crater chronology
 22 method. The presence of such asymmetries would bias the ages based on crater
 23 densities according to the location of the geologic unit. The Moon is subject
 24 to nonuniform cratering, since it is not massive enough to gravitationally ho-
 25 mogeneize encounter trajectories. Latitudinal asymmetries are produced by the
 26 anisotropy of encounter inclinations (Le Feuvre and Wieczorek, 2008), whereas

1 longitudinal asymmetries result from synchronous rotation since the relative
 2 encounter velocity, hence impact rate, are maximized at the apex of motion
 3 (e.g., Morota et al., 2005). In addition, the Earth may focus low inclination
 4 and velocity projectiles onto the nearside of the satellite or act as a shield at
 5 small separation distances.

6 Several studies have attempted to give estimates of the lunar cratering asym-
 7 metries. Wiesel (1971) used a simplified asteroid population, and Bandermann
 8 and Singer (1973) used analytical formulations based on strongly simplifying
 9 assumptions in order to calculate impact locations on a planet. These for-
 10 mulations did not allow to investigate any latitudinal effects. Wood (1973)
 11 numerically integrated the trajectories of ecliptic projectiles; Pinet (1985) nu-
 12 merically studied the asymmetries caused by geocentric projectiles that were
 13 potentially present early in the lunar history. Horedt and Neukum (1984),
 14 Shoemaker and Wolfe (1982), Zahnle et al. (1998) and Zahnle et al. (2001) all
 15 proposed analytical formulations for the apex/antapex effect, but the range of
 16 predicted amplitudes is very large (the first, in particular, claimed that this ef-
 17 fect is negligible for the Moon). Moreover, these four studies based their results
 18 on isotropic encounter inclinations. Gallant et al. (2009) numerically modeled
 19 projectile trajectories in the Sun-Earth-Moon system, and reported a signif-
 20 icant apex/antapex effect. In our study, we derive a semi-analytic approach
 21 for calculating cratering rates of synchronously locked satellites, and apply
 22 it to the Moon. This method yields results that are nearly identical to full
 23 numerical simulations, is computationally very rapid, and easily generalizable
 24 to other satellites.

25 The "asteroid to crater" modeling requires several steps to create synthetic
 26 crater distributions. First, one needs to know the impactor population as

1 a function of orbital elements, size and time. Second, impact probabilities
 2 are calculated over precession and revolution cycles of both the projectile
 3 and target, based on geometrical considerations (Öpik, 1951; Wetherill, 1967;
 4 Greenberg, 1982; Bottke and Greenberg, 1993). As these impact probabili-
 5 ties predict typically that a given planetary crosser will collide with a given
 6 planet over timescales of about 10 Ga, whereas the typical lifetime of these
 7 objects is thought to be a thousand times lower (Michel et al., 2005) as a
 8 result of ejection from the solar system or collision with another body, the
 9 calculated bombardment must be seen as the product of a steady-state pop-
 10 ulation, where vacant orbital niches are continuously reoccupied (Ivanov and
 11 Hartmann, 2007). Third, scaling laws derived from laboratory experiments
 12 and dimensional analyses are used to calculate the final crater size produced
 13 for given a impact condition (e.g., impactor size, velocity and cohesion of
 14 the target material), for which several different scaling laws have been pro-
 15 posed (Schmidt and Housen, 1987; Holsapple and Schmidt, 1987; Gault, 1974;
 16 Holsapple, 1993; Holsapple and Housen, 2007). Subsequent gravitational mod-
 17 ification of the transient cavity that gives rise to the final crater size have been
 18 deduced from crater morphological studies (Pike, 1980; Croft, 1985).

19 The rest of this paper is organized as follows. In the following section, we
 20 describe the employed orbital and size distribution of the impactor population.
 21 In section three, the necessary equations used in generating synthetic cratering
 22 rates are summarized; the full derivations are given in the appendix. In section
 23 four, we compare our synthetic lunar crater distribution with observations, we
 24 describe the lunar spatial asymmetries, and give the predicted planet/Moon
 25 cratering ratios. We also provide simple analytic equations that reproduce
 26 the predicted cratering asymmetries on the Moon, as well as the latitudinal

1 variations predicted for the terrestrial planets in Le Feuvre and Wieczorek
 2 (2008). Section five is dedicated to revising the crater chronology method.
 3 New age estimates are proposed for geologic units on the Moon, Earth, Venus
 4 and Mercury.

5 **2 Impactor population**

6 Let us denote a , e , i and d respectively the semi-major axis, eccentricity,
 7 inclination and diameter of those objects whose orbits can intersect the inner
 8 planets. The entire population can be written

$$n(> d, a, e, i) = \bar{n}(> 1) \times o(a, e, i) \times s(> d) , \quad (1)$$

9 where n can be expressed as the product of $\bar{n}(d > 1)$, the total number of
 10 objects with a diameter greater than 1 km; $o(a, e, i)$, the relative number of ob-
 11 jects with a given set of orbital elements, normalized so that $\int o(a, e, i) da de di =$
 12 1; and $s(> d)$, the normalized cumulative number of objects larger than a given
 13 diameter, such that $s(> 1 \text{ km}) = 1$. This formulation assumes that no corre-
 14 lations exist between the size of the object and its orbit, which is consistent
 15 with the observations of Stuart and Binzel (2004) for diameters ranging from
 16 $\sim 10 \text{ m}$ to $\sim 10 \text{ km}$.

17 *2.1 Orbital distribution*

18 The orbital distribution of near Earth-objects (NEOs) is taken from the model
 19 of Bottke et al. (2002), which provides a debiased estimate of the orbital dis-
 20 tribution of bolides that can potentially encounter the Earth-Moon system.

1 This model assumes that the NEO population is in steady-state, continu-
 2 ously replenished by the influx coming from source regions associated with
 3 the main asteroid belt or the transneptunian disk. The model was determined
 4 through extensive numerical integrations of test particles from these sources,
 5 and calibrated with the real population observed by the Spacewatch survey.
 6 The relative number of objects is discretized in orbital cells that spans 0.25
 7 AU in semi-major axis, 0.1 in eccentricity, and 5° in inclination.

8 In order to model the martian impact flux, we have amended this model by
 9 including the known asteroids that cross the orbit of Mars, but which are not
 10 part of the NEO population. These are taken from the database provided by E.
 11 Bowell (Lowell Observatory), that gives the orbit and absolute magnitude H
 12 of telescopic discoveries. We consider the population of $H < 15$ objects to be
 13 the best compromise between a sufficient number of objects (in order to avoid
 14 sparseness in the orbital space), and completeness. Their distribution as a
 15 function of perihelion is very similar in shape to brighter (hence larger) $H < 13$
 16 objects (see Le Feuvre and Wieczorek, 2008), the latter being large enough
 17 to ensure they do not suffer observational bias in the martian neighborhood.
 18 The $H < 15$ population is therefore considered as complete, and is scaled to
 19 match the modeled NEO population. From the relationship between absolute
 20 magnitude and geometric albedo of Bowell et al. (1989), and a mean albedo
 21 of 0.13 (Stuart and Binzel, 2004), $H < 15$ corresponds to $d > \sim 4$ km.

22 2.2 Size distribution

23 The size distribution of impactors is taken from a compilation of various esti-
 24 mates of the size-dependent impact rate on Earth, as shown in figure 1. This

1 compilation gathers atmospheric recordings of meteoroids and impact proba-
 2 bilities calculated with Öpik equations from debiased telescopic observations.
 3 Estimates from telescopic observations are those of Rabinowitz et al. (2000),
 4 Morbidelli et al. (2002), Harris, A. W. (2002) and Stuart and Binzel (2004).
 5 Estimates based on atmospheric recordings include Halliday et al. (1996),
 6 ReVelle (2001) and Brown et al. (2002). Concerning the LINEAR survey, esti-
 7 mates of Harris, A. W. (2002) have been scaled at large sizes to the estimates
 8 of Stuart and Binzel (2004). In contrast to Morbidelli et al. (2002) and Stuart
 9 and Binzel (2004), Rabinowitz et al. (2000) did not use a debiased albedo
 10 distribution, but rather a constant mean geometric albedo of 0.1 in order to
 11 convert their telescopic observations from magnitude to diameter at all sizes.
 12 Though small objects are expected to possess a larger albedo as they are gener-
 13 ally younger than large objects, we did not attempt to correct for this effect,
 14 since estimates of Rabinowitz et al. (2000) show a general agreement with
 15 other studies. In atmospheric flash estimates, masses have been deduced from
 16 kinetic energy, the latter being estimated from luminous energy. We convert
 17 kinetic energies of Brown et al. (2002) into diameters using a mean density
 18 of 2700 kg m^{-3} and a mean impact velocity of 20 km s^{-1} (Stuart and Binzel,
 19 2004). In order to increase the range of sizes in our compilation, and to reduce
 20 the statistical uncertainties associated with the larger objects, we have also
 21 included the size-frequency distribution of Mars-crossing objects with sizes
 22 greater than 4 km, and scaled these to the terrestrial impact rates of Stuart
 23 and Binzel (2004).

24 Various assumptions have led to all these estimates. Among them, the assumed
 25 impact velocity and bolide density are only of moderate influence. As an ex-
 26 ample, varying the density from 2700 to 2000 kg m^{-3} , or the mean impact

1 velocity from 20 to 17 km s⁻¹, changes the estimates of Brown et al. (2002)
 2 only by about 10 %. Of major influence are the luminous efficiency used to
 3 obtain kinetic energy from flashes (see Ortiz et al., 2006), and the debiasing
 4 process in the case of telescopic observations, which are difficult to assign a
 5 statistical uncertainty to. Consequently, we simply fit a 10th-order polynomial
 6 to the entire dataset, assuming each data is error free, and that the average
 7 combination of all estimates gives a good picture of the impactor population.

8 [Table 1 about here.]

9 We express the resulting analytic size-frequency distribution as the product
 10 of two terms: the normalized size distribution $\log s(> d) = \sum_{i=0}^{10} s_i (\log d_{\text{km}})^i$,
 11 whose coefficients are listed in table 1, and the Earth's impact rate for objects
 12 larger than 1 km, $\bar{\phi}_e(d > 1) = 3.1 \times 10^{-6} \text{ Ga}^{-1} \text{ km}^{-2}$. An overbar is appended
 13 to the Earth's impact rate symbol, denoting that this quantity is spatially av-
 14 eraged over the planet's surface. The size-frequency distribution of impactors
 15 is here assumed to be the same for all bodies in the inner solar system. The
 16 relative impact rates for these bodies with respect to Earth are calculated in
 17 Section 3 using the orbital distribution of the planet crossing objects.

18 [Fig. 1 about here.]

19 **3 From asteroids to craters**

20 Here we describe how is calculated the number of craters that form on the
 21 Moon and planets, per unit area and unit time, as a function of the crater
 22 diameter and location on the surface. We first need to calculate the encounter
 23 conditions generated by the impactor population, then the corresponding im-

1 pact rate and conditions (impact velocity and incidence angle), in order to
 2 finally obtain a cratering rate by the use of impact crater scaling laws. For the
 3 reader's convenience, derivations are given in the appendix.

4 3.1 *Encounter probability*

5 Following Öpik (1951), the assumptions under which an encounter is consid-
 6 ered to occur can be summarized as follows:

- 7 • An encounter between the target (Moon or planet) and impactor occurs
 8 at the geometrical point of crossing of the two orbits (the mutual node).
 9 The geometry of encounter is given by the relative velocity vector \mathbf{U} at this
 10 point, which is expressed here in a frame where the X-axis points towards
 11 the central body (planet or Sun), (XY) defines the target's orbital plane,
 12 and the Z-axis points upward.
- 13 • The relative encounter velocity does not account for the acceleration gener-
 14 ated by the mass of the target.
- 15 • The impactor, as seen by the target, is treated as if it were approaching from
 16 an infinite distance, under only the gravitational influence of the target.
 17 The encounter trajectory is therefore hyperbolic in the reference frame of
 18 the target.
- 19 • For a given \mathbf{U} , there are an infinite number of hyperbolic trajectories that
 20 can actually strike the target, that are distributed uniformly on a circle
 21 perpendicular to \mathbf{U} with a surface equal to the target's gravitational cross
 22 section.

1 These approximations hold as long as the radius of the target's Hill sphere
2 is large enough with respect to the target size. We performed three-body
3 numerical simulations that show that a factor of ten between the Hill sphere
4 and target radii suffices to ensure the validity of the above approximations.
5 For the terrestrial planets, this condition is largely verified. For the Moon, it
6 corresponds to a minimum Earth-Moon separation of ~ 17 Earth's radii.

7 In the case of planets in nearly circular orbits, the encounter geometry \mathbf{U} and
8 probability P (providing the two orbits intersect) are simply given by the well
9 known Öpik equations (Öpik, 1951). In order to account for the eccentricity
10 of the target (which is important for Mercury and Mars, but not for the
11 Earth), we use the improved formulation of Greenberg (1982) and Bottke and
12 Greenberg (1993). The probability is largest for low inclination encounters,
13 and for encounters occurring near the projectile's pericenter and apocenter.
14 Singularities of the encounter probability are avoided following Dones et al.
15 (1999). For a given orbital geometry, the encounter probability is proportional
16 to the gravitational cross section, whose radius is

$$\tau = R\sqrt{1 + \Gamma} , \quad (2)$$

17 where R is the target's radius and

$$\Gamma = 2 \frac{GM}{RU^2} \quad (3)$$

18 is the Safronov parameter, with G the gravitational constant and M the tar-
19 get's mass.

20 Note that the calculated impact probabilities are long-term averages over pre-
21 cession cycles of both the projectile and target (i.e., the longitude of node and
22 argument of pericenter can take any value between 0 and 2π). We account

1 for secular variations of the planetary orbital elements using the probability
 2 distributions given as a function of time in Laskar (2008). Our results are
 3 only sensitive to secular variations for Mars, and in the following, two values
 4 are quoted for this planet, that correspond to the present day value and to a
 5 long-term average (1 Ga and 4 Ga averages yield nearly identical results).

6 By calculating the encounter probability P and velocity \mathbf{U} associated with a
 7 given orbital element set (a, e, i) , by weighting this probability with the relative
 8 number of objects $o(a, e, i)$, and by summing over the entire planet-crossing
 9 population for each terrestrial planet, we build the probability distribution of
 10 the encounter conditions, $p(\mathbf{U})$, using bins of 1 km s^{-1} for each component of
 11 the encounter velocity. Analytically, we have

$$p(\mathbf{U}) = \frac{p'(\mathbf{U})}{\int_{\mathbf{U}} p'(\mathbf{U}) d\mathbf{U}} , \quad (4)$$

12 with

$$p'(\mathbf{U}) = \int_{\mathcal{D}} P(\mathcal{D}) o(a, e, i) \delta(\mathbf{U}(\mathcal{D}) - \mathbf{U}') d\mathcal{D} , \quad (5)$$

13 where the integration is performed over the 8-dimensional domain
 14 $\mathcal{D} = (U'_X, U'_Y, U'_Z, a, e, i, w_0, \Delta\Omega)$, with w_0 the target's argument of perihelion,
 15 $\Delta\Omega$ the difference between the target and projectile's longitudes of the ascend-
 16 ing node (see Greenberg, 1982), and δ the Kronecker function which equals 1
 17 when $\mathbf{U} = \mathbf{U}'$ and 0 otherwise. The impact rate relative to the Earth is

$$r = \frac{\int_{\mathbf{U}} p'(\mathbf{U}) d\mathbf{U}}{\int_{\mathbf{U}} p'_e(\mathbf{U}) d\mathbf{U}} . \quad (6)$$

18 where p'_e is calculated from equation 5 with the Earth being the target.

19 The lunar case requires a specific treatment, which is detailed in appendix A.2.
 20 For simplicity and without altering the results, it is assumed that the lunar
 21 orbit is circular about the Earth and possess a zero inclination with respect

1 to the ecliptic. We first calculate encounters probabilities P' and velocities
2 \mathbf{V} with the entire Earth-Moon system, whose expression is the same as for
3 the Earth, except that the gravitational cross section radius is replaced in the
4 Öpik equation by what we call here the lunar orbit cross section, defined as
5 (Zahnle et al., 1998)

$$\tau' = a_m \sqrt{1 + 2 \frac{v_m^2}{V^2}}, \quad (7)$$

6 where a_m and v_m are respectively the lunar semi-major axis and velocity. On
7 the cross sectional disk, the distance from the center is denoted by the impact
8 parameter b . Only when $b \leq \tau'$ is it possible for a hyperbolic orbit to impact the
9 Moon (note that the gravitational cross section of the Moon itself is accounted
10 for later in the calculation, see appendix A.2). The probability distribution of
11 encounter conditions $p(\mathbf{V})$ is first calculated according to this new definition
12 of the encounter probability. Then, the relative lunar encounter velocity \mathbf{U}
13 and probability P_m are derived analytically for each hyperbolic orbit crossing
14 the Earth-Moon system (equations A.19 – A.18, A.24 – A.25, A.30 – A.33).
15 The probability distribution of lunar encounter conditions, $p(\mathbf{U})$, is then de-
16 termined by integrating numerically P_m for all possible hyperbolic orbits of
17 each encounter \mathbf{V} , and for all encounter velocities. Similarly, the impact prob-
18 ability with Earth P_e is determined for each hyperbola, and the Moon/Earth
19 impact ratio r is calculated over all possible encounters. Mathematically, $p(\mathbf{U})$
20 and r are given by equations (A.34–A.36).

21 Note that there is a dependence of the lunar impact rate on the Earth-Moon
22 separation distance, a_m . This distance has evolved outward with time, and we
23 test various separation distances in the simulations. A major difference be-
24 tween our approach and previous investigations (Shoemaker and Wolfe, 1982;
25 Zahnle et al., 1998, 2001) is that the argument of pericenter of the hyperbolic

1 orbits is not assumed to precess uniformly within the Earth-Moon system,
 2 but is explicitly given by the encounter geometry. Our formulation allows to
 3 calculate explicitly lateral asymmetries in the lunar cratering rate.

4 3.2 Impact rate

5 Let us express the cumulative impact flux, that is the number of objects with
 6 diameters greater than d that hit the planet per unit time and area, as

$$\phi(> d, \lambda, \varphi) = \bar{\phi}(> d) \times \Delta\phi(\lambda, \varphi) , \quad (8)$$

7 where λ and φ are respectively the latitude and longitude, $\bar{\phi}(> d)$ is the
 8 spatially-averaged impact rate for projectiles larger than d , and $\Delta\phi(\lambda, \varphi)$ is the
 9 relative impact rate as a function of position, normalized to the global average.

10 Using our normalized impactor SFD, the average impact rate expresses as

$$\bar{\phi}(> d) = \bar{\phi}(> 1) s(> d) , \quad (9)$$

11 and $\bar{\phi}(d > 1)$ is obtained from the impact ratio between the target and Earth,
 12 r , and the terrestrial impact rate $\bar{\phi}_e(d > 1)$ as

$$\bar{\phi}(> 1) = r \bar{\phi}_e(> 1) . \quad (10)$$

13 The net spatial asymmetry $\Delta\phi(\lambda, \varphi)$ is found by integrating the spatial as-
 14 symmetries $\delta\phi(\lambda, \varphi, \mathbf{U})$ associated with each encounter geometry:

$$\Delta\phi(\lambda, \varphi) = \int_{\mathbf{U}} \delta\phi(\lambda, \varphi, \mathbf{U}) p(\mathbf{U}) d\mathbf{U} , \quad (11)$$

15 where $\delta\phi$ is given in appendix A.3 as a function of the Safronov parameter Γ
 16 and obliquity of the target (equations A.47 – A.49). The impact flux is homo-
 17 geneous for $\Gamma = \infty$, that is, for encounter velocities negligible with respect to

1 the target's surface gravitational potential (equation 3). On the other hand,
2 for $\Gamma = 0$, encounter trajectories are straight lines, and the impact flux is a
3 simple geometrical projection of the spatially uniform encounter flux (on a
4 plane perpendicular to the radiant) onto the target's spherical surface. The
5 associated impact velocities and incidence angles are calculated from equa-
6 tions (A.51) and (A.54). The impact velocity u is only dependent on U and
7 Γ , while the incidence angle θ further depends on position.

8 3.3 Cratering rate

9 To obtain cratering rates from impact rates, we need to convert the impactor
10 diameters into crater diameters. For this purpose, we use equations that have
11 been derived in the framework of π -scaling dimensional analysis (Holsapple
12 and Schmidt, 1987; Holsapple, 1993), where the transient crater is given as
13 a function of the projectile diameter, impact velocity, surface gravity and
14 projectile/target density ratio (see appendix A.4). It is assumed that only the
15 vertical component of the impact velocity, whose value is obtained from the
16 impact angle, contributes to the crater size (Pierazzo et al., 1997), though
17 other relations could be easily incorporated into this analysis. The scaling
18 equation and parameters are taken from the summary of Holsapple and Housen
19 (2007) for the case of porous and non-porous scaling. It will be seen that both
20 formation regimes are necessary to reconcile the impactor and crater SFDs.
21 We only consider craters that form in the gravity regime, where the tensile
22 strength of rock is negligible, that is, craters larger than a few hundred meters
23 in competent rock, and larger than a few meters in consolidated soils. An
24 increase of the transient crater diameter by wall slumping and rim formation is

1 accounted for as given in Melosh (1989, 253 pp.). Finally, large craters collapse
 2 due to gravity, becoming complex craters, and the relationship between simple
 3 and complex crater diameters is taken from Holsapple (1993). Putting this
 4 altogether, we obtain the relation $d(D, u, \theta)$ that gives the impactor diameter
 5 d as a function of the crater diameter D , impact velocity u and incidence
 6 angle θ (appendix A.4, equations (A.63 – A.59)). The impactor diameter d
 7 required to create a crater of size D is ultimately a function of λ , ϕ and \mathbf{U}
 8 (see equations A.51 and A.54).

9 The cratering rate, that is the number of craters larger than D that form at
 10 (λ, φ) per unit time and area, is

$$C(> D, \lambda, \varphi) = \int_{\mathbf{U}} \phi(> d, \lambda, \phi) p(\mathbf{U}) d\mathbf{U} , \quad (12)$$

11 where

$$d = d(D, \lambda, \phi, \mathbf{U}) . \quad (13)$$

12 For convenience, we separate the cratering rate into

$$C(> D, \lambda, \varphi) = \bar{C}(> D) \times \Delta C(> D, \lambda, \varphi) . \quad (14)$$

13 where $\bar{C}(> D)$ is the spatially averaged rate and $\Delta C(> D, \lambda, \varphi)$ is the rela-
 14 tive spatial variation. Note that ΔC depends on D , though in practice, this
 15 dependence is moderate (see next section).

1 4 Results

2 4.1 Crater size-frequency distributions

3 We first present our synthetic size-frequency distribution of lunar craters. Fol-
 4 lowing the terminology of Marchi et al. (2009), we refer to this as a model
 5 production function. We compare our model production function with the
 6 two standard measured production functions of Neukum (Neukum, 1983, 186
 7 pp.; Neukum and Ivanov, 1994) and Hartmann (Basaltic Volcanism Study
 8 Project, 1981; Hartmann, 1999). We note that the two are in good agreement
 9 over the crater diameter range from 300 m to 100 km, but differ between 2
 10 and 20 km, with a maximum discrepancy of a factor 3 at 5 km.

11 Using the traditional non-porous scaling relations and a standard target den-
 12 sity of 2800 kg m^{-3} , we calculate that 2.88×10^{-11} craters larger than 1 km
 13 would be created each year on the lunar surface by the present impactor pop-
 14 ulation. Using the time-dependence established by Neukum (1983, 186 pp.)
 15 that predicts a quasi-constant impact flux over the last $\sim 3 \text{ Ga}$, the Hartmann
 16 and Neukum production functions return respective values of 7.0×10^{-13} and
 17 8.2×10^{-13} , which are about forty times lower, implying that the present flux
 18 must be considerably larger than the time averaged value.

19 However, by using the porous scaling law instead, in order to account for
 20 the presence of megaregolith on the lunar surface, our calculated spatially
 21 averaged lunar cratering rate is

$$\bar{C}_m(D > 1) = 7.5 \times 10^{-13} \text{ yr}^{-1} \text{ km}^{-2} , \quad (15)$$

22 a value in excellent agreement with the two measured production functions

1 under the assumption of a constant impact flux over the last ~ 3 Ga.

2 Let us now reconcile the entire shape of the measured production functions
3 with the observed impactor population. As shown in figure 2, the two mea-
4 sured distributions are very well fitted by using the porous regime for small
5 craters ($D < 2$ km), and the non-porous regime for larger craters ($D > 20$
6 km). We model a simple smooth transition between the two regimes by con-
7 sidering that the impactor size d required to create a crater of diameter D is a
8 linear combination of the sizes required from the porous and non-porous scal-
9 ing relations, the influence of each regime depending on the depth of material
10 excavated by the crater. The depth of excavation z_T is about 1/10 of the tran-
11 sient crater diameter D_T , and does not seem to depend on target properties
12 (Melosh and Ivanov, 1999). The impactor size is averaged over the depth of
13 excavation:

$$d = \frac{1}{z_T} \int_0^{z_T} d_z(z) dz , \quad (16)$$

14 where d_z is the impactor size required by the material at depth z , given by
15 the porous regime at the surface, by the non-porous regime at depths larger
16 than a given "megaregolith thickness" T , and by a linear combination between
17 $z = 0$ and $z = T$:

$$d_z(z) = \frac{1}{T} ((T - z) d_p + z d_{np}) \text{ for } z \leq T , \quad (17)$$

$$d_z(z) = d_{np} \quad \text{for } z \geq T ,$$

18 with d_p and d_{np} the impactor diameters respectively required from the porous
19 and non-porous regimes. In the calculation of d_{np} , the target density is set to
20 2800 kg m^{-3} (solid rocks), whereas we assume in calculating d_p that the density
21 of the porous material is 2500 kg m^{-3} , based on Bondarenko and Shkuratov
22 (1999, abstract no. 1196) who inferred an upper regolith density comprised

1 between 2300 and 2600 kg m⁻³ from correlations between the surface regolith
 2 thickness and the Soderblom's crater parameter (Soderblom and Lebofsky,
 3 1972). We note that given the simplicity of our crater-scaling procedure in the
 4 transition zone, the correspondance between T and the actual megaregolith
 5 thickness should not be expected to be exact.

6 As shown in figure 2, our model reproduces both the Hartmann and Neukum
 7 production functions within the 100 m – 300 km diameter range, for respective
 8 values of T equal to 250 and 700 m, respectively. For these diameter ranges,
 9 the maximum discrepancy between our model and the Neukum production
 10 function is only 30 % at 200 m, and always less than 20 % for craters larger
 11 than 500 m. Below 100 m, we note that our model is in reasonable agreement
 12 with the Neukum production function, and we leave the implications for the
 13 contribution of secondary craters to further investigations. The model pro-
 14 duction function proposed by Marchi et al. (2009) is also shown in figure 2. A
 15 detailed comparison with this latter study is given in the discussion section.

16 [Fig. 2 about here.]

17 The use of porous scaling was first suggested by Ivanov (2006) (see also Ivanov,
 18 2008; Ivanov and Hartmann, 2007), and is a natural consequence of a highly
 19 fractured megaregolith on airless bodies. Also natural is to expect that the
 20 thickness of the megaregolith will depend upon both age and local geology.
 21 We note that the need for a transition regime falls within the diameter range
 22 where the measured production functions differ the most (excluding very large
 23 craters). We suspect that this is partially a result of the Hartmann produc-
 24 tion function being based on crater counts performed solely over mare units,
 25 whereas the Neukum production function also includes older highlands ter-

1 rains (Neukum et al., 2001a).

2 Estimated megaregolith thicknesses are roughly consistent with seismic mod-
 3 els of the lunar crust (e.g., Warren and Trice, 1977; Lognonné et al., 2003)
 4 that generally predict reduced seismic velocities for the upper km, which is
 5 attributed to an increased porosity and fractures. Furthermore, seismic data
 6 at the Apollo 17 landing site, overlaid by mare basalt, indicates that the upper
 7 250 / 400 m show a very low P-wave velocity with respect to the deeper basalt
 8 (Kovach and Watkins, 1973; Cooper et al., 1974), the lower estimate being in
 9 agreement with our calculated megaregolith depth of 250 m for the Hartmann
 10 production function. Finally, Thompson et al. (1979) show by analysis of radar
 11 and infrared data (which are dependent on the amount of near surface rocks)
 12 that craters overlying highlands show different signatures for craters greater
 13 and less than 12 km, and that mare craters down to 4 km in diameter possess
 14 a similar signature to that of highlands craters greater than 12 km. They at-
 15 tribute this difference to the presence of a pulverized megaregolith layer that
 16 is thicker in the older highlands than the younger mare.

17 By the use of a porous regime dictated by the properties of a megaregolith,
 18 our model production function reproduces the measured crater distributions
 19 in shape and in the absolute number of craters formed over the past 3 Ga,
 20 under the assumption of a constant impact flux. We caution that our simple
 21 formulation of the porous / non-porous transition does not account for the
 22 temporal evolution of the megaregolith and that the inferred megaregolith
 23 thicknesses are only qualitative estimates.

24 The present Earth-Moon distance has been used in the above calculation of
 25 the lunar cratering rate, and temporal variations in the lunar semimajor axis

could, in principle, modify the Earth/Moon impact ratio and encounter velocity distribution with the Moon. Nevertheless, it is found in our simulations that, for a lunar semi-major axis as low as 20 Earth radii, the average lunar cratering rate is changed by less than 3%. This implies that both the shielding and gravitational focusing of projectiles by the Earth are of very moderate effects, especially since the Moon is believed to have spent the vast majority of its history beyond 40 Earth radii.

[Table 2 about here.]

Our globally averaged planetary cratering rates $\bar{C}(> D)$ are fitted by 10th-order polynomials for the Moon and inner planets. The coefficients (with units of $\text{yr}^{-1} \text{ km}^2$) are listed in table 2. Since the megaregolith thickness is not necessarily the same on each planet, and may depend on the age and geology of the surface, coefficients are given for the two scaling regimes ($T = \infty$ and $T = 0 \text{ km}$) for diameters between 0.1 and 1000 km (except for the Earth and Venus, where only non-porous scaling is given). A linear transition simpler than ours can be used by defining two threshold diameters, D_p and D_{np} , such that the porous and non-porous regime applies alone respectively below D_p and above D_{np} . The cratering rate in the transition regime is then calculated as $C(> D) = C_p(> D_p) + \frac{C_{np}(> D_{np}) - C_p(> D_p)}{D_{np} - D_p} (D - D_p)$, where C_p and C_{np} are given in table 2 in the porous and non-porous columns, respectively. Note that the martian cratering rate is sensitive to the eccentricity of the planet, since the number of potential impactors increases dramatically as this planets gets closer to the Main Asteroid Belt (Le Feuvre and Wieczorek, 2008; Ivanov, 2001). In addition to calculating the present day martian cratering rate, we also used the probability distribution of the martian eccentricity provided by Laskar (2008) to calculate an average over the past 1 Ga (note that this value

1 is nearly insensitive for longer averages).

2 Planetary size-frequency distributions are generally expressed with respect to
3 the lunar one. This is done by defining the size-dependent quantity R_c , which
4 is the cratering ratio with respect to the Moon,

$$R_c(> D) = \frac{\bar{C}(> D)}{\bar{C}_m(> D)} . \quad (18)$$

5 For illustrative purpose, R_c is shown for the inner planets in figure 3 by assum-
6 ing that craters with diameters less than 10 km form in a porous soil on both
7 the planet and Moon, while craters with greater sizes form in solid rocks (ex-
8 cept for the Earth and Venus where only the non-porous regime is used). Note
9 that R_c can be easily calculated from equation 18 and table 2 for a different
10 (and more realistic) transition between porous and non-porous regimes.

11 [Fig. 3 about here.]

12 [Fig. 4 about here.]

13 The mean impact velocity on the Moon is calculated to be $\bar{u}_m = 19.7$ km
14 s^{-1} . The full probability distribution of impact velocities for each planet is
15 shown in figure 4. The quantities $\bar{\phi}/\bar{\phi}_m$, \bar{u}/\bar{u}_m and g/g_m , that give the relative
16 impact flux, impact velocity and surface gravity with respect to the Moon,
17 are given in table 3 for the inner planets. Mars experiences a high impact rate
18 with respect to the Moon (about 3) due to its proximity to the main asteroid
19 belt. In comparison, the martian cratering ratio is reduced (between about
20 0.5 and 2.5) because the impact velocity on Mars is significantly lower than
21 on the Moon, requiring larger (and hence less numerous) impactors to create
22 a crater of a given size. Mercury exhibits also a high impact rate, and the
23 impact velocity is about twice as large as on the Moon, resulting in a high

1 value of the cratering ratio R_c , comprised between 2 and 4. The impact rate
2 is larger on the Earth and Venus than on the Moon, as these planets possess a
3 higher gravitational attraction. Their higher surface gravities compensate the
4 differences in impact velocities with the Moon, and R_c is comprised between
5 0.5 and 1.5 for the Earth and between 1 and 2 for Venus.

6 [Table 3 about here.]

7 4.2 Spatial variations

8 The relative spatial cratering variations on the Moon, $\Delta C(> D, \lambda, \varphi)$, are
9 shown in figure 5 for the present Earth-Moon distance of about 60 Earth
10 radii, and for crater diameters larger than 1 km. The cratering rate varies
11 from approximately -20% to $+25\%$ with respect to the global average. It is
12 minimized at about $(\pm 65^\circ N, 90^\circ E)$, whereas the maximum, which is a factor
13 1.5 higher, is located at the apex of motion $(0^\circ N, 90^\circ W)$.

14 [Fig. 5 about here.]

15 Two effects conjugate to give such a distribution. First, a latitudinal effect,
16 detailed in Le Feuvre and Wieczorek (2008), comes from the higher propor-
17 tion of low inclination asteroids associated with the higher probabilities of low
18 inclination encounters. The pole/equator ratio is 0.80. Second, a longitudinal
19 apex/antapex effect comes from the synchronous rotation of the Moon and
20 the higher relative encounter velocities at the apex. The lunar orbital velocity
21 is added to the projectile velocity for impacts at the apex, whereas it is sub-
22 tracted at the antapex. The apex/antapex ratio is 1.37. We note that there is
23 a negligible nearside/farside effect: the nearside experiences the formation of

1 about 0.1% more craters than the farside. The Earth does indeed concentrate
2 very low inclination (and moderate velocity) projectiles onto the lunar near-
3 side, but these are not numerous enough to influence the global distribution.

4 The lateral cratering variations depend on the crater size since the size-
5 frequency distribution of impactors $s(> d)$ is not a simple power law, and
6 the impact conditions are not everywhere the same. Nevertheless, the maxi-
7 mum/minimum cratering ratio varies only by about 5% for D ranging from
8 30 m to 300 km. Consequently, for the following discussion, we shall consider
9 that $\Delta C(> D, \lambda, \varphi) \simeq \Delta C(> 1, \lambda, \varphi)$.

10 For smaller Earth-Moon distances a_m , the apex/antapex effect increases as
11 the lunar velocity increases. Between 20 and 60 Earth radii, this dependency
12 is fit by the simple equation

$$C(\text{apex})/C(\text{antapex}) = 1.12 e^{-0.0529 \frac{a_m}{R_e}} + 1.32, \quad (19)$$

13 where R_e is the Earth radius. Over this range of Earth-Moon separations,
14 latitudinal variations and the nearside/farside effect are found to vary by less
15 than 1%. These calculations assume that the lunar obliquity stayed equal to
16 its present value in the past.

17 Figure 6 plots the relative cratering rate ΔC as a function of the angular
18 distance from the apex of motion for the present Earth-Moon distance, and
19 compares this with the counts of rayed craters with diameters greater than
20 5 km given in Morota et al. (2005). Rayed craters are younger than about
21 1 Ga (Wilhelms et al., 1987), which should correspond to an Earth-Moon
22 separation distance very close to the present one (Sonett and Chan, 1998;
23 Eriksson and Simpson, 2000). As is seen, the model compares favorably to the

1 data.

2 [Fig. 6 about here.]

3 We note that the impact rate exhibits nearly the same behavior as the cra-
4 tering rate, but with a reduced amplitude. The pole/equator ratio is 0.90,
5 whereas the apex/antapex ratio is 1.29. The latitudinal cratering variations
6 are enhanced with respect to the impact rate variations, as the mean impact
7 angle and impact velocity are smaller at the poles than at the equator (re-
8 spectively by 2.5 degrees and 500 m/s), requiring a larger projectile to create
9 the same crater size. As large projectiles are less numerous than small ones,
10 the impact rate at the poles is smaller than the cratering rate (Le Feuvre and
11 Wieczorek, 2008). This is also true for the apex/antapex asymmetry, as the
12 average impact velocity is 500 m/s higher at the apex than at the antapex.
13 However, the increase is moderate, as the mean impact angle is only about
14 1.5 degree smaller.

15 It is seen in figure 7 that our predicted apex/antapex effect differs from that
16 of Zahnle et al. (2001). These authors describe their variations of the impact
17 rate as a function of γ , the angular distance to the apex, as

$$\Delta\phi(\gamma) = \left(1 + \frac{v_m}{\sqrt{2v_m^2 + \bar{V}^2}} \cos \gamma\right)^2, \quad (20)$$

18 where $\bar{V} \simeq 19 \text{ km s}^{-1}$ is the mean encounter velocity with the Earth-Moon
19 system. We are able to reproduce their analytical solution, but only under
20 the condition where we force the encounter inclinations with respect to the
21 lunar orbit plane to be isotropic in space. These authors used Öpik equations
22 (Shoemaker and Wolfe, 1982) for hyperbolic orbits that were assumed to pre-
23 cess uniformly inside the planet-moon system. We nevertheless point out that

1 Zahnle et al. (2001) applied equation (20) to the moons of Jupiter, where this
2 approximation might be valid.

3 [Fig. 7 about here.]

4 We next provide analytical solutions for the relative variations of both the im-
5 pact and cratering rates on the Moon. We also give solutions for the latitudi-
6 nal variations presented on the terrestrial planets in Le Feuvre and Wieczorek
7 (2008). Two values are quoted for Mars, one that corresponds to its present
8 obliquity and eccentricity and the other to averaged results using variations
9 over 3 Ga as given in Laskar et al. (2004) (see Le Feuvre and Wieczorek, 2008).
10 Spatial variations in the impact flux and cratering rate are parameterized by
11 a sum a spherical harmonic functions

$$\Delta C(\lambda, \varphi) = \sum_{l=0}^{\infty} \sum_{m=-l}^l C_{lm} Y_{lm}(\lambda, \varphi) , \quad (21)$$

12 where Y_{lm} is the spherical harmonic function of degree l and order m , C_{lm} is
13 the corresponding expansion coefficient, and (λ, φ) represents position on the
14 sphere in terms of latitude λ and longitude φ , respectively. The real spherical
15 harmonics are defined as

$$Y_{lm}(\lambda, \varphi) = \begin{cases} P_{lm}(\sin \lambda) \cos m\varphi & \text{if } m \geq 0 \\ P_{l|m|}(\sin \lambda) \sin |m|\varphi & \text{if } m < 0, \end{cases} \quad (22)$$

16 and the corresponding unnormalized Legendre functions are listed in Table 4.
17 Many of the expansion coefficients are nearly zero since the cratering rate
18 is symmetric about both the equator and the axis connecting the apex and
19 antapex of motion. Only the most significant coefficients are listed in Tables 5
20 and 6, which for most cases reproduce the data to better than 0.2%. The

1 coefficients for the latitudinal variations on the terrestrial planets are listed in
2 Tables 7 and 8.

3 [Table 4 about here.]

4 [Table 5 about here.]

5 [Table 6 about here.]

6 [Table 7 about here.]

7 [Table 8 about here.]

8 **5 Crater chronology**

9 Neukum et al. (2001a) (see also Neukum, 1983, 186 pp.; Strom and Neukum,
10 1988; Neukum and Ivanov, 1994) established empirically the following rela-
11 tionship between the number of craters with diameters greater than 1 km and
12 the age of the geologic unit:

$$\bar{N}(D > 1, t) = a(e^{bt} - 1) + c t, \quad (23)$$

13 where $\bar{N}(D > 1, t)$ is given per 10^6 km^2 , t is the age expressed in Ga, and
14 $a = 5.44 \times 10^{-14}$, $b = 6.93$ and $c = 8.38 \times 10^{-4}$. This relationship is essentially
15 linear over the last 3.3 Ga (constant cratering rate in time) and approximately
16 exponential beyond. The data used to construct this empirical curve are ob-
17 tained from radiometric ages of the Apollo and Luna rock samples, compared
18 to the crater density covering the associated geologic unit. We emphasize that
19 no agreed upon calibration data exist between 1 and 3 Ga and beyond 3.9
20 Ga (Stöffler and Ryder, 2001). We also note that equation (23) was originally

1 obtained using age estimates of the highland crust and Nectaris impact basin,
2 both of which are disputed and considerably older than 3.9 Ga.

3 Accounting for our calculated spatial variations, we first convert the measured
4 crater density at a given site, $N(D > 1, \lambda, \varphi)$, into the corresponding spatially
5 averaged quantity:

$$\bar{N}(D > 1) = N(D > 1, \lambda, \varphi) / \Delta C(D > 1, \lambda, \varphi) . \quad (24)$$

6 The cratering asymmetry ΔC is given in table 2, and we use the function that
7 corresponds to the present Earth-Moon separation for cratered surfaces that
8 are less than 1 Ga (consistent with the tidal deposit data of Sonett and Chan
9 (1998)). We choose a Earth-Moon separation of 40 Earth radii for units that
10 are older than 3 Ga (based on the tidal deposits data of Eriksson and Simpson
11 (2000)). This lunar semimajor axis value corresponds to a lunar orbital velocity
12 twice as large as the present one. We further assume that the lunar obliquity
13 was equal to its present value (nearly zero) for the entire time between 3.9 Ga
14 and the present.

15 The data used to calibrate the crater density versus age relationship are listed
16 in table 9, along with their corrections accounting for spatial variations in the
17 cratering rate. We use the crater density and ages values quoted in Stöffler and
18 Ryder (2001). We did not attempt to fit crater distributions with our model
19 production function to re-estimate $N(D > 1)$ values, since our model already
20 reproduces very well the Neukum production function that was used to esti-
21 mate this quantity. For the case of very young calibration surfaces, we suspect
22 that a thinner megaregolith might change the crater distribution with respect
23 to the Neukum production function at sizes larger than one kilometer, but,
24 for small exposure times, the largest observed craters are below this diameter

1 value. Based on the data and interpretations of Norman (2009), we exclude
2 the Nectaris basin from consideration, as it is possible that samples assigned
3 to this basin have instead an Imbrium provenance. We thus assume that the
4 Descartes formation is not Nectaris ejecta, but rather Imbrium ejecta with an
5 age of 3.85 Ga. We also exclude the Crisium basin from the fit, due to the
6 uncertain provenance of samples dated at the Luna 20 site. Finally, we use
7 the recent crater counts performed on Copernicus deposits by Hiesinger et al.
8 (2010, abstract no 1533) with high-resolution Lunar Reconnaissance Orbiter
9 images, which agree with a constant impact flux during the last 800 Ma, in
10 contrast to previous studies.

11 As seen in table 9, the spatial correction is in general moderate, since the cali-
12 bration terrains are located in the central portion of the nearside hemisphere,
13 far from the extrema of the spatially-dependent cratering rate. Nevertheless,
14 we point out that after correction, the Apennines, Fra Mauro and Descartes
15 formations, which are all Imbrian in age, exhibit nearly the same globally av-
16 eraged crater density, which is consistent with our assignment of an Imbrium
17 origin to the Descartes formation, as recently suggested by Norman (2009)
18 (see also Haskin et al., 1998).

19 We perform a new fit of the calibration point, using the same functional form
20 as in equation 23. Our resulting best parameters are

$$\begin{aligned} a' &= 1.893 \times 10^{-26} \\ b' &= 14.44 \\ c' &= 7.960 \times 10^{-4}, \end{aligned} \tag{25}$$

21 and our proposed curve is shown in figure 8, along with the curves proposed by

1 Neukum et al. (2001a) and Marchi et al. (2009). It is seen that our model favors
 2 a longer period of nearly constant impact flux (up to about 3.5 Ga), and that
 3 the agreement with the calibration points is improved. Crisium basin is also
 4 plotted (but was not included in the fit) for the tentative age of 3.895 given by
 5 Swindle et al. (1991, abstract no 1229), showing an excellent agreement with
 6 our model.

7 We note that the only calibration point that is not well fit to our relationship
 8 is the "young" group of basalts at the Apollo 11 landing site (point 9 in figure
 9 8). As discussed in Stöffler and Ryder (2001), four different flow units having
 10 distinct compositions and ages were sampled at this site, with ages of 3.58, 3.7,
 11 3.8, and 3.85 Ga. Previously measured crater densities were assigned to the
 12 3.58 and 3.8 Ga age groups, and we acknowledge the possibility that one, or
 13 perhaps both, of these assignments could possibly be in error. As an example,
 14 we note that if the 3.7 Ga age were assigned to the younger crater density
 15 that it would lie directly on our best fit line. In contrast, if the older crater
 16 density were assigned the 3.7 Ga age, this would require a different form to
 17 the fit between 3.41 and 3.75 Ga. Given the discrepancy of the 3.58 Ga crater
 18 density, ages derived from our crater chronology between 3.41 and 3.75 Ga
 19 should be used with caution.

20 Figure 8 also shows the range of bias that could occur if spatial variations
 21 are not taken into account in the crater chronology method. Radiometric ages
 22 obtained from future missions, or crater count data from images, that are far
 23 from the Apollo and Luna sampling sites might need to have their associ-
 24 ated local crater densities corrected by a factor up to $\sim 25\%$ to obtain the
 25 corresponding globally averaged value. Since the age/density relationship is
 26 approximatively linear for the last 3.5 Ga, ages could be biased by the same

amount as the spatial variations. Maximal variations in apparent ages would correspond to geologic units located at the apex or at $(\pm 65^\circ N, 90^\circ E)$. If one geologic unit were located at $(0^\circ N, 90^\circ W)$ and another at $(\pm 65^\circ N, 90^\circ E)$, and if both surfaces formed at 2 Ga, there would be about 900 Ma separating their apparent ages.

[Fig. 8 about here.]

[Table 9 about here.]

The number of craters larger than D that accumulate on a given planet, at the location (λ, φ) , and over a period of t Ga, is

$$N(> D, \lambda, \varphi, t) = C(> D, \lambda, \varphi) \times T(t) , \quad (26)$$

where the temporal dependency is

$$T(t) = \frac{a' (e^{b't} - 1) + c' t}{a' (e^{b'} - 1) + c'} , \quad (27)$$

and a' , b' and c' are given in equation 25. The dating of a planetary geologic unit is performed by finding the value of t that allows the best fit between $N(D, \lambda, \varphi, t)$ and the data.

At a given location (λ, φ) (note that φ plays a role only in the lunar case and that, apart from Mars where the cratering rate is expected to be 30 % less at the equator than at the pole, the latitudinal effect on the terrestrial planets is less than 10%), the best age is found by solving the linear least-square problem as a function of $T(t)$: $N_{obs}(> D_k) = C(> D_k, \lambda, \varphi) \times T(t)$, where $N_{obs}(> D_k)$ are the K measured cumulative crater densities with $k \in [1, K]$. Each data possesses an uncertainty $\sigma_k = \sqrt{N_{obs}(> D_k)}/A$, where A is the area where

1 craters have been counted. The solution (e.g., Tarantola 2001) is given by

$$T(t) = \frac{\sum_{k=1}^K C(> D_k, \lambda, \varphi) N_{obs}(> D_k) / \sigma_k^2}{\sum_{k=1}^K C^2(> D_k, \lambda, \varphi) / \sigma_k^2} \quad (28)$$

2 The a posteriori uncertainty is given by

$$\delta T(t) = \left(\sum_{k=1}^K \frac{C^2(> D_k, \lambda, \varphi)}{\sigma_k^2} \right)^{-\frac{1}{2}}. \quad (29)$$

3 The best age t (in Ga) and its uncertainty are finally determined from $T(t) \pm$
4 $\delta T(t)$.

5 We next show an application of our procedure by estimating new ages of key
6 geologic units on the Moon, Earth, Venus and Mercury. Figure 9a shows our
7 synthetic lunar SFD fitted to crater counts performed over the Orientale basin
8 (data from Neukum et al. (2001a)). The crater SFD is shown in R-plot form,
9 $R(> D) = D^3 \frac{dN(> D)}{dD}$, where changes in slope are emphasized with respect
10 to a reference cumulative distribution having a power-law slope of -2. We use
11 a best-fitting megaregolith thickness of 500 m, and exclude in the fit craters
12 smaller than 1.5 km in diameter that have reached saturation level. We find
13 an age of 3.73 ± 0.01 Ga. The difference with Neukum et al. (2001a), who
14 quoted an age of 3.70, lies principally in the updated coefficient values of
15 the calibration curve. Without accounting for spatial cratering variations, the
16 age would have been estimated to be 3.75 Ga. The bias in age from spatial
17 cratering variations is here moderate, as we are in the exponential part of the
18 calibration curve.

19 On Earth, Hughes (2000) used a nearest neighbors technique and known crater
20 ages to calculate the size-dependent formation rate of craters over the last
21 125 ± 20 Ma. The best fit between our model production function and the
22 estimates of Hughes (2000) is for an age of 138 ± 6 Ma (figure 9b), in excellent

1 agreement with a constant impact flux over this period. Craters smaller than
 2 15 km in diameter were not included in the fit, being depleted as a consequence
 3 of erosional processes (note that the megaregolith thickness was obviously set
 4 to 0 in this calculation). Our result implies that craters larger than about 10-
 5 20 km have not been erased by erosional processes over the last 100 Ma. We
 6 also fit our model to the crater distribution of a number of North American
 7 and European Phanerozoic cratons that have been independently estimated
 8 by Grieve and Dence (1979) to be 375 Ma old on average. Neukum and Ivanov
 9 (1994) noted that the crater chronology, once applied to this crater population,
 10 returns an age of about 700 Ma. Our best fit corresponds to an age of 390 ± 75
 11 Ma, in agreement with Grieve and Dence (1979).

12 Using crater counts derived from the Magellan mission, the average age of
 13 the Venusian surface has generally been estimated to be between 650 and
 14 750 Ma (Neukum and Ivanov, 1994; McKinnon et al., 1997; Korycansky and
 15 Zahnle, 2005). We fit our model distribution to the data, excluding craters
 16 smaller than 25 km in diameter: their depletion with respect to the model is
 17 attributed to atmospheric shielding. Our estimate, based on the use of the
 18 non-porous scaling alone, is shown in figure 9c, and corresponds to an age
 19 of 240 ± 13 Ma (figure 9c), significantly younger than other estimates. The
 20 difference lies principally in the impactor population used in the calculations.
 21 In particular, both Korycansky and Zahnle (2005) and McKinnon et al. (1997)
 22 used the Venus-crossing population estimated by Shoemaker et al. (1990),
 23 which produces an impact rate that is significantly higher than our value
 24 calculated from the NEO model of Bottke et al. (2002). This high impact rate
 25 is compensated in their study by a very efficient atmospheric shielding model
 26 that has the effect of decreasing the proportion of small craters. In particular,

1 the number of 30 km craters is reduced by about a factor 5 between their
 2 airless and atmosphere-shielded simulations in order to fit the data, whereas
 3 our airless model fits the crater distribution at that size, suggesting that the
 4 atmosphere is of negligible effect. Neukum and Ivanov (1994) assumed that the
 5 mean impact velocity on Venus is 19 km s^{-1} (we calculate 25 km s^{-1}), and that
 6 the projectile flux at infinity was the same for Venus and the Moon. Moreover,
 7 our venusian size-frequency distribution is not of the same shape as in Neukum
 8 and Ivanov (1994), because it was not constructed from the lunar production
 9 function, where porous megaregolith decreases the proportion of small craters,
 10 but rather directly from the impactor size distribution. We finally note that
 11 our inferred age is more similar to the estimate of Strom et al. (1994), who
 12 calculated the global surface of Venus to be 290 Ma old.

13 [Fig. 9 about here.]

14 Figure 9d shows crater counts performed on Mercury, both on plains interior
 15 to the Caloris basin and on the lineated Caloris basin sculpture (Fassett et al.,
 16 2009). Our best fits are respectively for megaregolith thicknesses of 250 m and
 17 900 m, and for ages of 3.30 ± 0.3 and 3.73 ± 0.2 Ga. According to Fassett
 18 et al. (2009), the size-frequency distribution of craters on the lineated sculp-
 19 ture (resulting from the basin formation) should be more representative of the
 20 Caloris basin formation time than the distribution measured on the Caloris
 21 rim, that exhibits a loss of small craters due to erosional processes and bad
 22 lighting conditions for crater counts, both being the consequences of the rim
 23 slope. Therefore, we attribute the age of 3.69 Ga to the Caloris basin. Our pre-
 24 ferred values are consistent with the interpretation that older surfaces present
 25 a thicker layer of megaregolith than younger ones. Moreover, the megaregolith
 26 appears to be thicker on Mercury than on the Moon, which is consistent with

1 the fact that Mercury has both impact rate and mean impact velocity that
 2 are about twice as great as for the Moon. Finally, we suggest the possibility
 3 that differences in crater size-frequency distribution between pre- and post-
 4 LHB surfaces may partially be explained by megaregolith thickness variations
 5 rather than changes in the impactor size distribution, the latter hypothesis
 6 being supported by Strom et al. (2005).

7 **6 Discussion**

8 Here we compare our calculations with published results, and discuss the sen-
 9 sitivity of our model to various parameters. Our present Earth/Moon impact
 10 ratio and mean lunar impact velocity are calculated to be, respectively, 1.58
 11 and 19.7 km s^{-1} . This is comparable to the values of Stuart and Binzel (2004)
 12 (respectively 1.61 and 19.3 km s^{-1}), who used Öpik calculations for an isolated
 13 Moon possessing an Earth-like orbit about the Sun. These authors used the
 14 NEO population of Stuart (2001), estimated from the debiased observations of
 15 the LINEAR survey, and calculated the cratering rate on the Earth and Moon
 16 using various scaling laws. They did not account for a porous megaregolith.

17 Gallant et al. (2009) used numerical simulations to estimate lunar asymme-
 18 tries. From the NEO population of Bottke et al. (2002), they calculated the
 19 probability of encounter with the Earth-Moon system with Öpik probabilities,
 20 and used a 4-body (projectile, Moon, Earth and Sun) numerical approach to
 21 calculate the encounter trajectory, starting at 0.02 AU from the Earth. They
 22 reported a mean lunar impact velocity of 20 km s^{-1} . Our analytical approach
 23 yields consistent values with their predicted apex/antapex cratering ratio as
 24 a function of the Earth-Moon distance: our leading/trailing hemispheric ratio

1 is 1.17 for the present lunar semi-major axis $a_m = 60$ Earth radii, and 1.20
 2 for $a_m = 40$ Earth radii, while Gallant et al. (2009) gave respectively 1.15
 3 and 1.18. Their latitudinal effect is found to be 10%, whereas ours is 20%.
 4 The difference is due to the crater scaling employed: Gallant et al. (2009) did
 5 not include the effect of the impact angle on the crater diameter, while we
 6 consider that only the vertical component of the impact velocity contributes
 7 to the crater size. By ignoring the effect of impact angle, we indeed obtain
 8 a similar latitudinal effect of $\sim 10\%$ (see Le Feuvre and Wieczorek, 2008).
 9 The "vertical component" scaling appears to be the safest assumption for a
 10 single target body, though the impact angle dependence of the average crater
 11 efficiency may vary from planet to planet (see Collins et al. 2009, Elbeshausen
 12 2009). Nevertheless, this angle dependence is of negligible influence in the cal-
 13 culation of planetary cratering rate ratios with respect to the Moon, and only
 14 affects the amplitude of the cratering asymmetries on a given body. Gallant
 15 et al. (2009) also estimated the terrestrial impact rate as a function of local
 16 time (see figure 9 of their paper). Although it is not the purpose of this paper,
 17 we note here that our semi-analytical approach reproduces their results.

18 Recently, Marchi et al. (2009) proposed a revised crater chronology. The main
 19 differences with our approach (excluding the assumption of spatially uniform
 20 cratering rates in the latter) are the following:

- 21 • We use the orbital distribution of near-Earth objects of Bottke et al. (2002),
 22 modified for Mars, which is assumed to be in steady state and independent
 23 of bolide size. Marchi et al. (2009), in contrast, use a subset of this model
 24 based on orbital integrations of test particles coming from only the 3:1 and
 25 ν_6 resonances. Furthermore, the relative importance of these two sources is

- not the same as in the final debiased model of Bottke et al. (2002).
- We assume that the size frequency distribution of objects impacting the planets is the same for all planets and that the probability of an object impacting a planet is independent of size. In contrast, in Marchi et al. (2009), the size frequency distribution differs for each planet and is dependent on how much time the impactors spend in the asteroid belt. Furthermore, the impact probabilities are assumed to depend upon the projectile size.
 - In the impact crater scaling relations, we use $K=1.17$ for impacts in water for the gravity regime, whereas Marchi et al. (2009) use $K=0.93$ for impacts in wet soils and rock in the strength regime (though employed in the general scaling relationship that contains both strength and gravity terms).
 - When converting transient crater diameters to final crater diameters, we use a multiplicative factor of 1.56 as suggested by Melosh (1989, 253 pp.) and Melosh (1998), whereas Marchi et al. (2009) assume that the transient crater diameter is equivalent to the final simple crater diameter for their preferred impact scaling law that is based on the equations in Holsapple and Housen (2007).
 - Both studies treat the case of impact crater scaling in the porous megaregolith differently. We use a linear transition from porous (i.e., "sand or cohesive soils" from Holsapple and Housen (2007)) to nonporous scaling to fit either the Neukum or Hartmann production functions. In contrast, Marchi et al. (2009) place the transition between porous and nonporous scaling at projectile diameters of 0.5 km (corresponding to a crater diameter of about 5 km), and additionally use an average strength parameter in their impact crater scaling relationship that depends on crater size.

It is difficult to quantify how each of these differences affect the final crater

size-frequency distribution on a planetary object, and hence the derived ages of a surface. Nonetheless, we note that the different bolide size-frequency distributions and the different crater scaling laws could be significant. As an example, if Marchi et al. (2009) were to have used the same crater scaling constants and to have multiplied their transient crater diameters by the same factor as us, this would have increased their predicted crater densities by about a factor of 5. Excluding these factors from our analysis would have decreased our crater densities by the same factor.

Regardless of these differences, we note that our model production function is in closer agreement with the Neukum production function than that proposed by Marchi et al. (2009). In particular, our crater densities differ by a factor of 1.1 and 0.8 at crater diameters of 1 and 50 km, respectively (1.3 and 0.7 with respect to the Hartmann production function), whereas for Marchi et al. (2009) the respective factors are about 1.5 and 0.3 (1.7 and 0.2 with respect to the Hartmann production function). Though a factor of 5 increase in crater densities would improve their fit to the Neukum production function at large crater diameters, the misfit would be significantly worse for small craters.

It should be noted that, according to Stewart and Valiant (2006), morphological analysis of young Martian craters combined with theoretical crater scaling relationships implies a factor of about 1.4 for modification of the transient cavity by wall slumping and rim uplift (in addition to gravity collapse of complex craters), whereas Melosh (1989, 253 pp.) suggested a factor of 1.56. Using the Stewart and Valiant (2006) factor would make our crater densities differ at most by 40 % from the Neukum production function for crater sizes between 100 m and 300 km. Using an impactor density of 2000 instead of 2700 kg m⁻³ would produce the same effect. Given the uncertainties in both the transient

1 cavity modification factor and the impactor densities, we favor our previous
2 estimate, that is in closer agreement with the observed production functions.

3 The density and porosity of the lunar megaregolith are not known with any
4 certainty. It is likely that porosity reduces the density of the first few hundred
5 meters of the lunar crust. Nevertheless, the subsurface study of the Ries crater
6 on Earth (Pohl et al., 1977) indicates that the density reduction is moderate.
7 We used a value of 2500 kg m^{-3} for the upper density of the megaregolith in
8 the calculation of the impact crater sizes, based on Bondarenko and Shkuratov
9 (1999, abstract no. 1196). Regardless, we note that taking an extreme value
10 of 2000 kg m^{-3} would still produce a broad agreement with the Neukum
11 production function, with a maximum discrepancy of 50 % for crater sizes
12 between 500 m and 300 km.

13 We test the sensitivity of our calculated lunar cratering asymmetries by using
14 the NEO orbital distribution given by telescopic observations only, either for
15 diameters larger than 1 km or 4 km, instead of the orbital model provided
16 by Bottke et al. (2002). Using the $d > 4 \text{ km}$ population leads to a strong
17 enhancement of lunar latitudinal asymmetries. The pole/equator is in this
18 case equal to 0.56, due to the high proportion of these objects in the ecliptic
19 plane. For the $d > 1 \text{ km}$ population, latitudinal variations are less than 1 %
20 with respect to the average. These observations suggest that the observation of
21 low inclination objects with $d < 1 \text{ km}$ is incomplete, which is not unexpected
22 since this type of detection is more difficult than for high inclination objects.
23 Regardless, in both cases, the apex/antapex ratio does not change significantly.

24 The porous regime is required so that the calculated lunar production rate
25 for craters smaller than about 10 km matches the Hartmann and Neukum

1 production functions. As reported by Strom et al. (2005), counts of post-LHB
 2 lunar craters seem to be adequately fit by the observed NEO size-frequency
 3 distribution and the sole use of the non-porous cratering regime. An alterna-
 4 tive possibility is that young geologic units that are less impacted, possess a
 5 thinner porous megaregolith layer than older units, and that this has acted
 6 to change the apparent size-frequency distribution of lunar craters with time.
 7 The evolution of megaregolith thickness with time remains to be determined,
 8 as well as the equivalent thickness on Mercury and Mars, for which the distri-
 9 bution of craters smaller than a few kilometers is still to be better understood
 10 before our model can be confidently used: Mercury may exhibit an abundance
 11 of large secondaries, whereas the presence of subsurface ice may significantly
 12 reduce the upper porosity of the martian crust.

13 Finally, we caution that our model may be inaccurate for periods prior to 3.5
 14 Ga, both because of the Late Heavy Bombardment and a possible reorientation
 15 of the Moon (Wieczorek and Le Feuvre, 2009). Our study is generalizable
 16 to different impactor populations or planetary reorientations, but the affects
 17 of these events are difficult to assess without a better knowledge. Waiting
 18 in particular for a suitable dynamical model for small bodies in the early
 19 solar system, we have applied our cratering model to times prior to 3.5 Ga,
 20 based on the following considerations. First, the size-frequency distributions
 21 of craters on the oldest lunar terranes are potentially explained by varying the
 22 megaregolith thickness, without the need for a different impactor population.
 23 Second, even if the cratering asymmetries would have been modified by these
 24 events, the influence of spatial variations on the age estimates is very moderate
 25 for times prior to 3.5 Ga (which correspond to the exponential part of the
 26 chronology curve).

7 Conclusions

We have presented a complete set of equations that allows to calculate the cratering rate as a function of crater size and location, on the Moon and inner planets. Spatial variations of the cratering rate are calculated semi-analytically, hence considerably faster than by the use of a fully numerical method. The approach is generalizable to any other planet or moon, providing the orbital and size distributions of impactors are known. For our purpose, the NEO orbital distribution model of Bottke et al. (2002) has been used, and the size distribution of bolides has been fitted to a compilation of various estimates (Rabinowitz et al., 2000; Morbidelli et al., 2002; Harris, A. W., 2002; Stuart and Binzel, 2004; Halliday et al., 1996; ReVelle, 2001; Brown et al., 2002).

Significant cratering asymmetries, both latitudinal and longitudinal, are found on the lunar surface. These are the result of both the high proportion of low inclination encounters and the synchronous rotation of the satellite. If the resulting bias in the estimate of absolute ages is in general moderate with respect to other uncertainties associated with the crater chronology method, and therefore should not invalidate most of the published ages, this systematic effect could be as large as 500 Ma for geologic units of 2 Ga close to ($0^\circ N, 90^\circ W$) or ($\pm 65^\circ N, 90^\circ E$), and should be accounted for when determining relative ages between different surfaces.

Our synthetic size-frequency distribution of lunar craters matches the standard production functions (see Neukum et al., 2001a), providing that a porous megaregolith is accounted for at crater diameters smaller than a few kilometers. The absolute number of craters formed during the last 3 billion years

1 is consistent with a constant impact flux and the present day cratering rate.
 2 The shape of the size-frequency distribution is predicted to be time-dependent,
 3 since older surfaces would possess a thicker layer of fractured megaregolith.

4 We have provided an updated crater chronology curve that excludes some
 5 debated calibration points based on geologic considerations, and accounts for
 6 the spatially-dependent cratering rate at the calibration units. The proposed
 7 curve favors a longer period of constant impact flux, extending up to 3.5 Ga
 8 ago. We have also given polynomial fits for the crater size-frequency distrib-
 9 utions calculated on Mercury, Venus, the Earth and Mars, allowing the easy
 10 calculation of age estimates on these planets.

11 Our model is consistent with the terrestrial cratering records (Hughes, 2000;
 12 Grieve and Dence, 1979) for the last 400 Ma. For the Moon, we find that
 13 the age of the Orientale impact basin is 3.73 Ga, which is 30 Ma older than
 14 previous estimates. This corresponds to a shorter Late Heavy Bombardment,
 15 since it is generally considered that the Caloris basin marks the end of this
 16 event. On Mercury, we attribute the same age to the Caloris basin. We finally
 17 estimate the venusian surface to be only 240 Ma old on average, which is 2–3
 18 times younger than most previous estimates. Such an age is similar to the
 19 oldest oceanic crust on Earth and implies that volcanic resurfacing occurs on
 20 Venus at only a slightly reduced rate as on Earth.

21 **Acknowledgements**

22 We thank B. Ivanov and S. Werner for constructive reviews and comments
 23 that improved this manuscript. We thank W. Bottke and A. Morbidelli for

1 their orbital distribution model. MLF has been supported by a grant from the
2 Centre National d'Etudes Spatiales (CNES) and acknowledges the Laboratory
3 of Planetology and Geodynamics of Nantes, France, for hosting and fruitful
4 discussions. Figures were created using the Generic Mapping Tools of Wessel
5 and Smith (1991).

6 **A Derivations**

7 Here we describe in detail how we compute the lunar and planetary cratering
8 rates. We start by recalling how to obtain orbital elements in the 2-body
9 problem, which is required for calculating hyperbolic trajectories of objects as
10 they encounter a planet or Moon. Second, we adapt Öpik impact probabilities,
11 originally intended for planets, to the case of a moon in synchronous rotation.
12 Third, we derive equations to calculate the impact rate as a function of position
13 on the target surface (planet or moon). Finally, we recall the equations that
14 allow us to calculate crater diameters from impactor diameters and impact
15 conditions.

16 *A.1 Orbital elements*

17 Consider a massless particle (our projectile) orbiting around a massive body
18 M (our target) isolated in space (two-body problem), described in a Cartesian
19 coordinate system (oxyz) whose origin is the center of the target, with $\hat{\mathbf{x}}$, $\hat{\mathbf{y}}$ and
20 $\hat{\mathbf{z}}$ the associated unit vectors. The plane (oxy) is chosen as the orbital plane of
21 the target body. All the following definitions can be found in standard celestial
22 mechanics textbooks (e.g., Murray and Dermott, 2000, 606 pp.). The distance

1 of the projectile to the center of the target is

$$r = \frac{p}{1 + e \cos f} , \quad (\text{A.1})$$

2 where p is the semilatus rectum, e the eccentricity and f the true anomaly.

3 The pericentre distance ($f = \pi$) is given by

$$q = \frac{p}{1 - e} . \quad (\text{A.2})$$

4 The semilatus rectum is

$$p = \frac{h^2}{GM} , \quad (\text{A.3})$$

5 where M is the mass of the target body, and the specific angular momentum,

6 constant and perpendicular to the projectile orbital plane, is

$$\mathbf{h} = \mathbf{r} \times \dot{\mathbf{r}} . \quad (\text{A.4})$$

7 The eccentricity vector is

$$\mathbf{e} = \frac{\dot{\mathbf{r}} \times \mathbf{h}}{GM} - \frac{\mathbf{r}}{r} , \quad (\text{A.5})$$

8 and the eccentricity is simply $e = \|\mathbf{e}\|$. Alternatively, the eccentricity can be

9 calculated from the particle's specific energy ξ as

$$e = \sqrt{2\xi \left(\frac{h}{GM} \right)^2 + 1} . \quad (\text{A.6})$$

10 The inclination of the orbit with respect to the (oxy) plane is calculated from

$$\cos i = \frac{\mathbf{h} \cdot \hat{\mathbf{z}}}{h} , \quad (\text{A.7})$$

11 where $i \in [0, \pi]$. The nodal vector, that points towards the ascending node, is

$$\mathbf{n} = \hat{\mathbf{z}} \times \frac{\mathbf{h}}{h} , \quad (\text{A.8})$$

1 and the longitude of the ascending node, measured from (ox) , is calculated
2 from

$$\cos \Omega = \frac{\mathbf{n} \cdot \hat{\mathbf{x}}}{n} , \quad (\text{A.9})$$

3 and

$$\sin \Omega = \frac{\mathbf{n} \cdot \hat{\mathbf{y}}}{n} . \quad (\text{A.10})$$

4 The argument of pericentre ω is given by

$$\cos \omega = \frac{\mathbf{n} \cdot \mathbf{e}}{n e} , \quad (\text{A.11})$$

5 with

$$\omega \in [0, \pi] \text{ if } \mathbf{e} \cdot \hat{\mathbf{z}} \geq 0 , \quad (\text{A.12})$$

$$\omega \in]\pi, 2\pi[\text{ otherwise .}$$

6 The true anomaly is calculated from

$$\cos f = \frac{\mathbf{e} \cdot \mathbf{r}}{e r} , \quad (\text{A.13})$$

7 with

$$f \in [0, \pi] \text{ if } \mathbf{r} \cdot \dot{\mathbf{r}} \geq 0 , \quad (\text{A.14})$$

$$f \in]\pi, 2\pi[\text{ otherwise .}$$

8 Finally, defining Θ as the angle that the projectile makes with respect to the
9 line of nodes, we have

$$\Theta = f + \omega , \quad (\text{A.15})$$

10 and the projectile crosses the target's orbital plane at $\Theta = 0$ and $\Theta = \pi$,
11 respectively on an ascending and descending trajectory.

1 A.2 Encounter probabilities with the Moon

2 Let us call \mathbf{V} the encounter conditions with the Earth-Moon system, calcu-
 3 lated as explained in section 3.1, and expressed in a right-handed coordinate
 4 frame where the origin is at the center of the Earth, the x -axis point towards
 5 the Sun, (xy) is the Earth orbital plane, and the z -axis points upward. The
 6 symmetry induced by the lunar rotation about the Earth makes the problem
 7 only dependent on V and V_z . Let us take $V_y = 0$ and $V_x \leq 0$. Consider also
 8 the frame $(x'yz')$, where the x' -axis and \mathbf{V} are antiparallel. This frame is use-
 9 ful to express the specific angular momentum and eccentricity vector, since
 10 it avoids complications due to the initial position of the projectile at infinity.
 11 The rotation matrix from $(x'yz')$ to (xyz) is therefore

$$M = \begin{pmatrix} \frac{\sqrt{V^2 - V_z^2}}{V} & 0 & \frac{V_z}{V} \\ 0 & 1 & 0 \\ -\frac{V_z}{V} & 0 & \frac{\sqrt{V^2 - V_z^2}}{V} \end{pmatrix}. \quad (\text{A.16})$$

12 The encounter velocity and initial position of the projectile on the cross section
 13 disk, perpendicular to x' , expressed in $(x'yz')$ as

$$\mathbf{V} = \begin{pmatrix} -V \\ 0 \\ 0 \end{pmatrix}_{(x'yz')}, \quad \mathbf{r} = \begin{pmatrix} \infty \\ b \cos \alpha \\ b \sin \alpha \end{pmatrix}_{(x'yz')}, \quad (\text{A.17})$$

14 where b is the impact parameter and α defines the angular position on the
 15 cross section disk with respect to the y -axis.

From these initial conditions, the specific angular momentum of the projectile and eccentricity vector are easily obtained by equations (A.4) and (A.5), and expressed in the (xyz) frame by the use of the rotation matrix M (equation A.16). The norm of the eccentricity vector is

$$E = \sqrt{1 + \left(\frac{b}{a_m}\right)^2 \left(\frac{V}{v_m}\right)^4}, \quad (\text{A.18})$$

where a_m and v_m are the lunar semi-major axis and orbital velocity. The inclination with respect to the system orbit plane (xy) is (equation A.7)

$$I = \cos^{-1} \left(\sqrt{1 - \frac{V_z^2}{V^2}} \cos \alpha \right). \quad (\text{A.19})$$

Note that the eccentricity E and inclination I of the hyperbolic trajectory have been capitalized in order to distinguish them from the orbital elements e and i for elliptic orbits about the Sun. The pericenter distance q is (equation A.2)

$$q = a_m(E - 1) / \left(\frac{V}{v_m}\right)^2, \quad (\text{A.20})$$

the nodal vector is calculated with equation (A.8), and the argument of pericenter is finally expressed by equation (A.11) as

$$\cos \omega = \frac{\frac{V_z}{V} \sqrt{E^2 - 1} - \sqrt{1 - \frac{V_z^2}{V^2}} \sin \alpha}{E \sin I}. \quad (\text{A.21})$$

For an intersection to occur between the projectile and Moon, the projectile must cross the lunar orbit plane at a distance a_m from the Earth. Since V_z is indifferently positive or negative (Öpik, 1951), the symmetry with respect to the system orbit plane allows to restrict ourselves to one of the nodes, here chosen to be the descending node. In this case, $\Theta = \pi$ implies (equation A.15)

$$\cos f = -\cos \omega, \quad (\text{A.22})$$

1 and $r = a_m$ gives (equation A.1)

$$\cos f = \frac{q/a_m(1+E) - 1}{E} . \quad (\text{A.23})$$

2 By using the two above equations, with E , q and $\cos \omega$ expressed as a function
3 of \mathbf{V} , b and α from equations (A.18), (A.20) and (A.21), it is found that the
4 value of the impact parameter that allows intersection is

$$b_m = \frac{a_m}{2} \left(\sqrt{\left(\frac{V_z}{V \sin I}\right)^2 + 4 \left(1 + \frac{\tan \alpha}{\tan I}\right) \left(\frac{v_m}{V}\right)^2} - \frac{V_z}{V \sin I} \right) . \quad (\text{A.24})$$

5 and that there is only one value of b that allows intersection on the descending
6 node for a given angular position on the lunar orbit cross section α .

7 For hyperbolic orbits, the relative encounter velocity with the Moon \mathbf{U} is given
8 in Shoemaker and Wolfe (1982) as a function of q , e and I . For the appropriate
9 value of the impact parameter that allows collision, we rewrite these equations
10 as

$$\begin{cases} U^2 = V^2 + v_m^2 - 2v_m U_Y , \\ U_X^2 = V^2 \left(1 - \left(\frac{b_m}{a_m}\right)^2\right) + 2v_m^2 , \\ U_Y = V \frac{b_m}{a_m} \cos I - v_m , \\ U_Z^2 = V^2 \left(\frac{b_m}{a_m}\right)^2 \sin^2 I . \end{cases} \quad (\text{A.25})$$

11 where \mathbf{U} is expressed in the frame (XYZ) attached to the center of the Moon,
12 where the X-axis point towards the Earth, the Y-axis points to the antapex of
13 motion, (XY) defines the Lunar orbital plane, and the Z-axis points upward.
14 Since we have restricted ourselves to the descending node, U_Z is negative. But
15 symmetry requires that U_Z is positive with the same probability. The sign of
16 U_X is to be discussed in the following.

1 Öpik probabilities assume that the argument of pericenter ω takes any value
 2 between 0 and 2π with an equal probability. While this is appropriate for
 3 elliptic orbits that precess about the Sun, the ω of our hyperbolic trajectory is
 4 constrained by the geometry of encounter with the Earth-Moon system. The
 5 encounter probability with the Moon can be expressed as follows

$$P_m = \frac{\Delta(b^2)}{\tau'^2} \times \frac{\Delta t}{T_m}, \quad (\text{A.26})$$

6 where $\Delta(b^2)$ is the interval around b_m^2 that allows the minimum distance be-
 7 tween the projectile's and target's orbits to be smaller than the gravitational
 8 cross section radius of the Moon, τ_m . We are interested in the square of b here,
 9 whose probability distribution on the lunar orbit cross section is uniform. The
 10 ratio $\frac{\Delta(b^2)}{\tau'^2}$ corresponds to the fraction in space allowing the collision, since b^2
 11 can take values between 0 and τ'^2 . Similarly, the term $\frac{\Delta t}{T_m}$ is the fraction of
 12 time that allows the collision, T_m being the orbital period of the Moon. This
 13 latter term is given by (see Öpik, 1951):

$$\frac{\Delta t}{T_m} = \frac{\tau_m}{4a_m} \frac{U}{\sqrt{U^2 - U_Y^2}}. \quad (\text{A.27})$$

14 At this point we need to express $\Delta(b^2)$ in terms of the relevant variables of
 15 our problem. At the node, $\Theta = \pi$; denoting L_{max} the distance between $r_{\Theta=\pi}$
 16 and a_m such as the minimum distance between the two orbits equals τ_m , we
 17 have

$$\frac{2L_{max}}{\Delta(b^2)} \simeq \left(\frac{\partial r_{\Theta=\pi}}{\partial b^2} \right)_{b=b_m}, \quad (\text{A.28})$$

18 with

$$L_{max} = \tau_m \sqrt{1 + U_X^2/U_Z^2}. \quad (\text{A.29})$$

19 Equations (A.27) and (A.29) come from the assumption that the projectile
 20 and Moon follow straight lines trajectories in the vicinity of the node, and

are demonstrated in Öpik (1951). Expressing $\left(\frac{\partial r_{\Theta=\pi}}{\partial b^2}\right)_{b=b_m}$ as a function of \mathbf{V} and α , inserting equation (A.29) into equation (A.28), and equations (A.28), (A.27) and (2) into equation (A.26), we finally get the impact probability with the Moon as

$$P_m = \frac{\tau_m^2}{a_m^2} \frac{U}{|U_Z|} \frac{v_m^2}{2v_m^2 + V^2} \frac{1}{\sin I} \frac{\left(\sin I + \sqrt{1 - \left(\frac{V_z}{V}\right)^2} \sin \alpha - \frac{V_z |U_Z|}{v_m^2 \sin I}\right)^2}{2 \sin I + 2 \sqrt{1 - \left(\frac{V_z}{V}\right)^2} \sin \alpha - \frac{V_z |U_Z|}{v_m^2 \sin I}}. \quad (\text{A.30})$$

If $U_X \leq 0$ and $q \leq R_e$ simultaneously, R_e being the radius of the Earth, a collision with the planet occurs, and P_m is set to 0 (the Moon cannot be impacted, as the sign of U_X indicates that the projectile has already cross the Earth). Denoting b_e the impact parameter corresponding to $q = R_e$ we have from equation A.20:

$$b_e = \sqrt{2R_e a_m \left(\frac{v_m}{V}\right)^2 + R_e^2}, \quad (\text{A.31})$$

and $q \leq R_e$ corresponds to $b_m \leq b_e$. The sign of U_X is known from

$$\begin{aligned} U_X &= -\sqrt{U_X^2} \text{ for } \sqrt{E^2 - 1} \sin \alpha / \tan I \geq 1 \\ U_X &= \sqrt{U_X^2} \text{ for } \sqrt{E^2 - 1} \sin \alpha / \tan I < 1 \end{aligned} \quad (\text{A.32})$$

where the first and second cases correspond respectively to an argument of pericenter comprised between 0 and π and between π and 2π (equation A.12). For instance, in the first case, the descending node is reached after the minimum distance to Earth, and the projectile is moving away from the Earth. Finally, the impact probability with Earth is given by

$$P_e = \frac{1}{2} \frac{b_e^2}{\tau'^2} - P_m, \quad (\text{A.33})$$

where the factor 1/2 comes from the restriction to one of the two possible

1 nodes. For a given encounter \mathbf{V} with the Earth-Moon system, P_m , \mathbf{U} and
 2 P_e are calculated for $\alpha \in [0, 2\pi]$. The probability distribution of the lunar
 3 encounter conditions is

$$p(\mathbf{U}) = \frac{p'(\mathbf{U})}{\int_{\mathbf{U}} p'(\mathbf{U}) d\mathbf{U}} , \quad (\text{A.34})$$

4 with

$$p'(\mathbf{U}) = \int_{\alpha=0}^{2\pi} \int_{\mathbf{U}'=0}^{\infty} \int_{\mathbf{V}} P_m(\alpha, \mathbf{V}) p(\mathbf{V}) \delta(\mathbf{U}(\alpha, \mathbf{V}) - \mathbf{U}') d\mathbf{V} d\mathbf{U}' d\alpha , \quad (\text{A.35})$$

5 where $p(\mathbf{V})$ is the probability distribution of the encounter distribution with
 6 the Earth-Moon system and δ is the Kronecker function. Finally, the Earth/Moon
 7 impact ratio is

$$r_e = \frac{\int_{\alpha=0}^{2\pi} \int_{\mathbf{V}} P_m(\alpha, \mathbf{V}) p(\mathbf{V}) d\mathbf{V} d\alpha}{\int_{\alpha=0}^{2\pi} \int_{\mathbf{V}} P_e(\alpha, \mathbf{V}) p(\mathbf{V}) d\mathbf{V} d\alpha} . \quad (\text{A.36})$$

8 *A.3 Impact rate as a function of position*

9 Each encounter \mathbf{U} generates an infinity of hyperbolic trajectories towards the
 10 target (moon or planet), initially uniformly distributed over the gravitational
 11 cross section at infinity. Let us call b the impact parameter and β the angular
 12 distance between a point on the target surface and the radiant. For a given
 13 target mass M and radius R , one value of b corresponds to one value of β .
 14 The impact rate at β is proportional to the area of the annulus $2\pi b db$
 15 divided by the elementary target surface $2\pi R^2 \sin \beta d\beta$. The total impact rate
 16 is proportional to the gravitational cross sectional area, $\pi\tau^2$, divided by the
 17 total area of the target surface $4\pi R^2$. The relative impact rate, normalized to
 18 the global average, is therefore

$$\delta\phi = \frac{(2\pi b db)/(2\pi R^2 \sin \beta d\beta)}{(\pi\tau^2)/(4\pi R^2)} = \frac{4}{\tau^2} \frac{b db}{\sin \beta d\beta} . \quad (\text{A.37})$$

1 We now have to express b as a function of β . By noting that $\beta = f_i - f_\infty$,
 2 where f_i is the projectile's true anomaly at the time of impact, and f_∞ is the
 3 initial true anomaly at infinity, we have

$$\begin{cases} \cos \beta = \cos(f_i) \cos(f_\infty) + \sin(f_i) \sin(f_\infty) , \\ \sin \beta = \sin(f_i) \cos(f_\infty) - \cos(f_i) \sin(f_\infty) . \end{cases} \quad (\text{A.38})$$

4 An impact occurs when $r = R$. The corresponding cosine of the true anomaly
 5 is (equation A.1)

$$\cos f_i = \frac{p/R - 1}{e} . \quad (\text{A.39})$$

6 Since the distance between the projectile and target is initially infinite, the
 7 cosine of the initial true anomaly is (equation A.1)

$$\cos f_\infty = -1/e. \quad (\text{A.40})$$

8 The true anomaly at infinity is negative (since $\mathbf{r}_\infty \cdot \mathbf{U}_\infty < 0$). This is also true
 9 for f_i , as the collision occurs necessarily before the projectile is at pericenter
 10 ($f = 0$). Therefore,

$$\sin f_i = -\sqrt{1 - \cos^2 f_i} \quad \text{and} \quad \sin f_\infty = -\sqrt{1 - \cos^2 f_\infty} . \quad (\text{A.41})$$

11 The specific angular momentum is given by equation (A.4)

$$h = b U . \quad (\text{A.42})$$

12 This allows to express the parameter of the conic as (equation (A.3),

$$p = \frac{b^2 U^2}{GM} . \quad (\text{A.43})$$

1 From equation (A.6), with an specific energy $\xi = U^2/2$, the eccentricity is

$$e = \sqrt{1 + \left(\frac{b U^2}{GM} \right)^2} . \quad (\text{A.44})$$

2 Using equations (A.44)–(A.38), the impact parameter b is found to be

$$b = R \frac{\tan(\beta/2)}{1 + \tan^2(\beta/2)} \left(1 + \sqrt{1 + \Gamma(1 + \tan^2(\beta/2))} \right) , \quad (\text{A.45})$$

3 and the maximum value of β is given for $b = \tau$ as

$$\cos \beta_{max} = -\frac{\Gamma}{2 + \Gamma} . \quad (\text{A.46})$$

4 Calculating $db/d\beta$ from the above equation, we get the relative impact flux as
5 a function of β from equation (A.37):

$$\delta\phi(\beta, \mathbf{U}) = \begin{cases} \frac{1+\cos\beta}{2(1+\Gamma)} \frac{1+\mu}{\mu} \times \\ \left[\mu^2 + \mu - (1+\mu) \frac{1-\cos\beta}{1+\cos\beta} \right] \text{ if } \beta \leq \cos^{-1} \left(-\frac{\Gamma}{2+\Gamma} \right) , \\ 0 \text{ if } \beta > \cos^{-1} \left(-\frac{\Gamma}{2+\Gamma} \right) , \end{cases} \quad (\text{A.47})$$

6 with

$$\mu = \sqrt{1 + \Gamma + \Gamma \frac{1 - \cos \beta}{1 + \cos \beta}} . \quad (\text{A.48})$$

7 The angular distance β is then simply expressed as a function of latitude λ
8 and longitude φ by calculating the scalar product between a given position
9 on the target and the radiant (equation A.44). Note that the dependency in
10 longitude φ corresponds to a target body in synchronous rotation. When it is
11 not the case, the flux is longitudinally uniform (the obliquity of the target is

1 taken into account at the end of this section). For a zero obliquity, we have

$$\cos \beta = (\cos \lambda \cos \varphi, \cos \lambda \sin \varphi, \sin \lambda) \times \frac{\mathbf{U}}{\|\mathbf{U}\|}. \quad (\text{A.49})$$

2 We finally need the impact velocity u and incidence angle with respect to the
3 surface, θ . The conservation of energy implies

$$\frac{U^2}{2} = \frac{u^2}{2} - \frac{GM}{R}, \quad (\text{A.50})$$

4 giving

$$u = U\sqrt{1 + \Gamma}, \quad (\text{A.51})$$

5 The specific angular momentum at the time of impact is (equation A.4)

$$h = R u \sin(\theta + \pi/2). \quad (\text{A.52})$$

6 The conservation of h allows identification with equation (A.42), giving

$$\cos \theta = b/\tau, \quad (\text{A.53})$$

7 and the impact angle is finally given as a function of β as

$$\theta = \cos^{-1} \left(\frac{1 + \mu}{2\sqrt{1 + \Gamma}} \sqrt{1 - \cos^2 \beta} \right). \quad (\text{A.54})$$

8 Let us finally account for the obliquity ϵ of the target. The obliquity reduces
9 spatial variations of the impact rate, since the target's sphere is moved under
10 the projectile flux by precession of the spin axis. Let us denote φ_ϵ the longitude
11 of the spin axis in the (XYZ) frame, and W the matrix

$$W = \begin{bmatrix} \cos^2 \varphi_\epsilon + \sin^2 \varphi_\epsilon \cos \epsilon & \cos \varphi_\epsilon \sin \varphi_\epsilon (1 - \cos \epsilon) & -\sin \varphi_\epsilon \sin \epsilon \\ \cos \varphi_\epsilon \sin \varphi_\epsilon (1 - \cos \epsilon) & \sin^2 \varphi_\epsilon + \cos^2 \varphi_\epsilon \cos \epsilon & \cos \varphi_\epsilon \sin \epsilon \\ \sin \varphi_\epsilon S_\epsilon & -\cos \varphi_\epsilon \sin \epsilon & \cos \epsilon \end{bmatrix}^{-1}, \quad (\text{A.55})$$

1 then the latitude and longitude (λ', φ') in the (XYZ) frame express as a
2 function of the geographic coordinates (λ, φ) as

$$\sin \lambda' = W_{31} \cos \lambda \cos \varphi + W_{32} \cos \lambda \sin \varphi + W_{33} \sin \lambda , \quad (\text{A.56})$$

3 and

$$\begin{aligned} \cos \varphi' &= \frac{W_{11} \cos \lambda \cos \varphi + W_{12} \cos \lambda \sin \varphi + W_{13} \sin \lambda}{\sqrt{1 - \sin^2 \lambda'}} , \\ \sin \varphi' &= \frac{W_{21} \cos \lambda \cos \varphi + W_{22} \cos \lambda \sin \varphi + W_{23} \sin \lambda}{\sqrt{1 - \sin^2 \lambda'}} . \end{aligned} \quad (\text{A.57})$$

4 The impact rate is finally given as a function of the geographic position as

$$\delta\phi(\lambda, \varphi) = \frac{1}{2\pi} \int_0^{2\pi} \delta\phi(\lambda'(\lambda, \varphi, \epsilon, \varphi_\epsilon), \varphi'(\lambda, \varphi, \epsilon, \varphi_\epsilon)) d\varphi_\epsilon , \quad (\text{A.58})$$

5 where the precession of the spin axis is simulated by φ_ϵ taking uniform values
6 between 0 and 2π .

7 A.4 Crater scaling

8 For our purpose, we express the projectile diameter d required to create a
9 crater with a given final diameter D , under given impact conditions. Let us
10 call D_s the final diameter of a simple crater. Large craters collapse due to
11 gravity, such that $D > D_s$. According to Holsapple (1993),

$$\begin{cases} D_s = D & \text{if } D < D_* , \\ D_s = 0.98 D_*^{0.079} D^{0.921} & \text{if } D \geq D_* , \end{cases} \quad (\text{A.59})$$

12 where D_* is a transition diameter believed to be approximately inversely pro-
13 portional to the surface gravity, and is about $D_{*m} = 8.5$ km for the Moon,

1 that is

$$D_* = \frac{g_m}{g} D_{*m} , \quad (\text{A.60})$$

2 where g_m is the lunar surface gravity.

3 Before wall slumping and rim formation, the diameter of the transient cavity
4 D_T is smaller than the final diameter of the simple crater D_s by a factor
5 $1.2 \times 1.3 = 1.56$ (Melosh, 1989, 253 pp.):

$$D_T = D_s / 1.56 . \quad (\text{A.61})$$

6 Denoting D_\perp the transient cavity for vertical impacts ($\theta = \pi/2$) we assume

$$D_\perp = D_T (\sin \theta)^{-2\nu_1} , \quad (\text{A.62})$$

7 that is, only the vertical component of the impact velocity has to be accounted
8 for. Other assumed functional dependencies on the incidence angle can easily
9 be used in place of equation (A.62).

10 In the gravity regime, where the tensile strength of rock is negligible, the
11 projectile diameter is finally given by Holsapple and Housen (2007) as

$$d = \left(K^{-1} D_\perp u^{-2\nu_1} g^{\nu_1} \left(\frac{\rho_0}{\rho} \right)^{\nu_2} \right)^{\frac{1}{1-\nu_1}} , \quad (\text{A.63})$$

12 with ρ and ρ_0 respectively the density of the projectile and target, and g the
13 surface gravity. The scaling parameter are taken from Holsapple and Housen
14 (2007) as $K = 1.17$, $\nu_1 = 0.22$ and $\nu_2 = 0.31$ for the non-porous gravity
15 scaling regime (impacts in water), and $K = 1.03$, $\nu_1 = 0.17$ and $\nu_2 = 0.332$
16 for the porous scaling. For a given crater diameter D , the impactor size d is
17 known from the successive use of the above equations, from equation (A.63)
18 to equation (A.59).

1 References

- 2 R. B. Baldwin. *The face of the Moon*. Univ. of Chicago Press, 1949.
- 3 L. W. Bandermann and S. F. Singer. Calculation of meteoroid impacts on
4 moon and earth. *Icarus*, 19:108–113, 1973.
- 5 Basaltic Volcanism Study Project. *Basaltic volcanism on the terrestrial plan-*
6 *ets*. Pergamon Press, Inc, New York, 1981.
- 7 N. V. Bondarenko and Y. G. Shkuratov. Thickness of lunar regolith and
8 Soderblom's crater parameter D_l. In *Proceedings of the 30th Lunar and*
9 *Planetary Science Conference*, 1999, abstract no. 1196.
- 10 W. F. Bottke and R. Greenberg. Asteroidal collision probabilities. *Geophys.*
11 *Res. Lett.* , 20:879–881, 1993.
- 12 W. F. Bottke, A. Morbidelli, R. Jedicke, J.-M. Petit, H. F. Levison, P. Michel,
13 and T. S. Metcalfe. Debaised orbital and absolute magnitude distribution
14 of the Near-Earth Objects. *Icarus*, 156:399–433, 2002.
- 15 E. Bowell, B. Hapke, D. Domingue, K. Lumme, J. Peltoniemi, and A. W.
16 Harris. Application of photometric models to asteroids. In R. P. Binzel,
17 T. Gehrels, and M. S. Matthews, editors, *Asteroids II*, pages 524–556. Univ.
18 of Arizona Press, Tucson, 1989.
- 19 P. Brown, R. E. Spalding, D. O. ReVelle, E. Tagliaferri, and S. P. Worden.
20 The flux of small near-Earth objects colliding with the Earth. *Nature*, 420:
21 294–296, 2002.
- 22 M. R. Cooper, R. L. Kovach, and J. S. Watkins. Lunar near-surface structure.
23 *Reviews of Geophysics and Space Physics*, 12:291–308, 1974.
- 24 S. K. Croft. The scaling of complex craters. *J. Geophys. Res.* , 90:828–842,
25 1985.
- 26 L. Dones, B. Gladman, H. J. Melosh, W. B. Tonks, H. F. Levison, and M. Dun-

- 1 can. Dynamical lifetimes and final fates of small bodies: orbit integrations
2 vs Öpik calculations. *Icarus*, 142:509–524, 1999.
- 3 K. A. Eriksson and E. L. Simpson. Quantifying the oldest tidal record: The
4 3.2 Ga Moodies Group, Barberton Greenstone Belt, South Africa. *Geology*,
5 28(9):831–834, 2000.
- 6 C. I. Fassett, J. W. Head, D. T. Blewett, C. R. Chapman, J. L. Dickson, S. L.
7 Murchie, S. C. Solomon, and T. R. Watters. Caloris impact basin: Exterior
8 geomorphology, stratigraphy, morphometry, radial sculpture, and smooth
9 plains deposits. *Earth Planet. Sci. Lett.*, 285:297–308, 2009.
- 10 J. Gallant, B. Gladman, and M. Čuk. Current bombardment of the earth-
11 moon system: Emphasis on cratering asymmetries. *Icarus*, 202:371–382,
12 2009.
- 13 D. E. Gault. Impact cratering. In R. Greeley and P. H. Schultz, editors, *A*
14 *Primer in Lunar Geology*, pages 137–175, 1974.
- 15 R. Gomes, K. Tsiganis, A. Morbidelli, and H. F. Levison. Origin of the cata-
16 clysmic late heavy bombardment period of the terrestrial planets. *Nature*,
17 435(7041):466–469, 2005.
- 18 R. Greenberg. Orbital interactions: a new geometrical formalism. *Astron. J.*,
19 87:184–195, 1982.
- 20 R. A. F. Grieve and M. R. Dence. The terrestrial cratering record. II - the
21 crater production rate. *Icarus*, 38:230–242, 1979.
- 22 I. Halliday, A. A. Griffin, and A. T. Blackwell. Detailed data for 259 fireballs
23 from the Canadian camera network and inferences concerning the influx of
24 large meteoroids. *Meteoritics and Planetary Science*, 31:185–217, 1996.
- 25 Harris, A. W. A New Estimate of the Population of Small NEAs. In *Bulletin*
26 *of the American Astronomical Society*, volume 34, page 835, 2002.
- 27 W. K. Hartmann. Martian cratering VI. Crater count isochrons and evidence

- 1 for recent volcanism from Mars Global Surveyor. *Meteoritics and Planetary*
2 *Science*, 34:167–177, 1999.
- 3 W. K. Hartmann and G. Neukum. Cratering chronology and the evolution of
4 Mars. *Space Sci. Rev.*, 96:165–194, 2001.
- 5 W. K. Hartmann, G. Ryder, L. Dones, and D. Grinspoon. The time-dependent
6 intense bombardment of the primordial Earth/Moon system. In R. M.
7 Canup, K. Righter, and 69 collaborating authors, editors, *Origin of the*
8 *Earth and Moon*, pages 493–512. Univ. of Arizona Press, Tucson, 2000.
- 9 L. A. Haskin, R. L. Korotev, K. M. Rockow, and B. L. Jolliff. The case for an
10 imbrium origin of the apollo th-rich impact-melt breccias. *Meteoritics and*
11 *Planetary Science*, 33:959–975, 1998.
- 12 H. Hiesinger, C. H. van der Bogert, J. H. Pasckertt, M. S. Robinson, K. Klemm,
13 D. Reiss, and Lroc Team. New crater size-frequency distribution measure-
14 ments for copernicus crater based on lunar reconnaissance orbiter camera
15 images. In *Proceedings of the 41st Lunar and Planetary Science Conference*,
16 2010, abstract no 1533.
- 17 K. A. Holsapple. The scaling of impact processes in planetary sciences. *Annu.*
18 *Rev. Earth Planet. Sci.*, 21:333–373, 1993.
- 19 K. A. Holsapple and K. R. Housen. A crater and its ejecta: An interpretation
20 of Deep Impact. *Icarus*, 187:345–356, 2007.
- 21 K. A. Holsapple and R. M. Schmidt. Point source solutions and coupling
22 parameters in cratering mechanics. *J. Geophys. Res.* , 92:6350–6376, 1987.
- 23 G. P. Horedt and G. Neukum. Cratering rate over the surface of a synchronous
24 satellite. *Icarus*, 60:710–717, 1984.
- 25 D. W. Hughes. A new approach to the calculation of the cratering rate of the
26 earth over the last 125 ± 20 myr. *Monthly Notices of the Royal Astronomical*

- 1 *Society*, 317(2):429–437, 2000.
- 2 B. A. Ivanov. Mars/Moon cratering rate ratio estimates. *Space Sci. Rev.*, 96:
- 3 87–104, 2001.
- 4 B. A. Ivanov. Earth/Moon impact rate comparison: searching constraints for
- 5 lunar secondary/primary cratering proportion. *Icarus*, 183:504–507, 2006.
- 6 B. A. Ivanov. Size-frequency distribution of asteroids and impact craters:
- 7 estimates of impact rate. In V. V. Adushkin and I. V. Nemchinov, editors,
- 8 *Catastrophic Events Caused by Cosmic Objects*, pages 91–116. Springer,
- 9 2008.
- 10 B. A. Ivanov and W. K. Hartmann. Exogenic dynamics, cratering and sur-
- 11 face ages. In Schubert G. and T. Spohn, editors, *Treatise on geophysics*,
- 12 volume 10, pages 207–242. Elsevier, 2007.
- 13 D. G. Korycansky and K. J. Zahnle. Modeling crater populations on Venus
- 14 and Titan. *Planet. and Sp. Sci.*, 53:695–710, 2005.
- 15 R. L. Kovach and J. S. Watkins. Apollo 17 seismic profiling: Probing the lunar
- 16 crust. *Science*, 180(1063-1064), 1973.
- 17 J. Laskar. Chaotic diffusion in the solar system. *Icarus*, 196:1–15, 2008.
- 18 J. Laskar, A. C. M. Correia, M. Gastineau, F. Joutel, B. Levrard, and P. Robu-
- 19 tel. Long term evolution and chaotic diffusion of the insolation quantities
- 20 of Mars. *Icarus*, 170:343–364, 2004.
- 21 M. Le Feuvre and M. A. Wieczorek. Nonuniform cratering of the terrestrial
- 22 planets. *Icarus*, 197:291–306, 2008.
- 23 P. Lognonné, J. Gagnepain-Beyneix, and H. Chenet. A new seismic model
- 24 of the moon: implications for structure, thermal evolution and formation of
- 25 the moon. *Earth and Planetary Science Letters*, 211:21–44, 2003.
- 26 S. Marchi, S. Mottola, G. Cremonese, M. Massironi, and E. Martellato. A new

- 1 chronology for the moon and mercury. *Astron. J.*, 137:4936–4948, 2009.
- 2 W. B. McKinnon, K. J. Zahnle, B. A. Ivanov, and H. J. Melosh. Cratering
3 on Venus: models and observations. In S. W. Bougher, D. M. Hunten, and
4 R. J. Philips, editors, *Venus II: Geology, Geophysics, Atmosphere, and Solar*
5 *Wind Environment*. Univ. of Arizona Press, Tucson, 1997.
- 6 H. J. Melosh. *Impact cratering: A geologic process*. Oxford University Press,
7 New York, 1989, 253 pp.
- 8 H. J. Melosh. Crater scaling program, 1998. URL [http://www.lpl.arizona.](http://www.lpl.arizona.edu/tekton/crater.html)
9 [edu/tekton/crater.html](http://www.lpl.arizona.edu/tekton/crater.html).
- 10 H. J. Melosh and B. A. Ivanov. Impact crater collapse. *Annual Review of*
11 *Earth and Planetary Sciences*, 27:385–415, 1999.
- 12 P. Michel, A. Morbidelli, and W. F. Bottke. Origin and dynamics of near
13 Earth objects. *Comptes Rendus Physiques*, 6:291–301, 2005.
- 14 A. Morbidelli, R. Jedicke, W. F. Bottke, P. Michel, and E. F. Tedesco. From
15 magnitudes to diameters: the albedo distribution of Near Earth Objects and
16 the Earth collision hazard. *Icarus*, 158:329–342, 2002.
- 17 T. Morota, T. Ukai, and M. Furumoto. Influence of the asymmetrical cratering
18 rate on the lunar cratering chronology. *Icarus*, 173:322–324, 2005.
- 19 C. D. Murray and S. F. Dermott. *Solar System Dynamics*. Cambridge Uni-
20 versity Press, UK, 2000, 606 pp.
- 21 G. Neukum. Meteoritenbombardement und datierung planetarer oberflächen.
22 Habilitation Dissertation. Ludwig-Maximilians-University of Munich. 1983,
23 186 pp.
- 24 G. Neukum and B. A. Ivanov. Crater size distributions and impact probabili-
25 ties on Earth from lunar, terrestrial-planet, and asteroid cratering data. In
26 T. Gehrels, M. S. Matthews, and A. M. Schumann, editors, *Hazards Due to*

- 1 *Comets and Asteroids*. Univ. of Arizona Press, Tucson, 1994.
- 2 G. Neukum, B. A. Ivanov, and W. K. Hartmann. Cratering records in the
3 inner Solar System in relation to the lunar reference system. *Space Sci.*
4 *Rev.*, 96:55–86, 2001a.
- 5 G. Neukum, J. Oberst, H. Hoffmann, R. Wagner, and B. A. Ivanov. Geologic
6 evolution and cratering history of Mercury. *Planet. Space Sci.*, 49:1507–
7 1521, 2001b.
- 8 M. D. Norman. The lunar cataclysm: Reality or 'mythconception'? *Elements*,
9 5(1):23–28, 2009.
- 10 E. J. Öpik. Collision probability with the planets and the distribution of
11 planetary matter. *Proc. R. Irish Acad. Sect. A*, 54:165–199, 1951.
- 12 J. L. Ortiz, F. J. Aceituno, J. A. Quesada, J. Aceituno, M. Fernández,
13 P. Santos-Sanz, J. M. Trigo-Rodríguez, J. Llorca, F. J. Martín-Torres,
14 P. Montañés-Rodríguez, and E. Pallé. Detection of sporadic impact flashes
15 on the Moon: Implications for the luminous efficiency of hypervelocity im-
16 pacts and derived terrestrial impact rates. *Icarus*, 184:319–326, 2006.
- 17 E. Pierazzo, A. M. Vickery, and H. J. Melosh. A reevaluation of impact melt
18 production. *Icarus*, 127:408–423, 1997.
- 19 R. J. Pike. Formation of complex impact craters — Evidence from Mars and
20 other planets. *Icarus*, 43:1–19, 1980.
- 21 P. Pinet. Lunar impact flux distribution and global asymmetry revisited.
22 *Astron. Astrophys.*, 151:222–234, 1985.
- 23 J. Pohl, D. Stoeffler, H. Gall, and K. Ernstson. The Ries impact crater. In
24 & R. B. Merrill D. J. Roddy, R. O. Pepin, editor, *Impact and Explosion*
25 *Cratering: Planetary and Terrestrial Implications*, pages 343–404, 1977.
- 26 D. Rabinowitz, E. Helin, K. Lawrence, and S. Pravdo. A reduced estimate of
27 the number of kilometre-sized near-Earth asteroids. *Nature*, 403:165–166,

- 1 2000.
- 2 D. O. ReVelle. Global infrasonic monitoring of large bodies. In B. Warmbein,
3 editor, *Proceedings of the Meteoroids 2001 Conference, Kiruna, Sweden*,
4 pages 483–489. ESA SP-495, Noordwijk: ESA Publications Division, 2001.
- 5 R. M. Schmidt and K. R. Housen. Some recent advances in the scaling of
6 impact and explosion cratering. *Intl. J. Impact Eng.*, 5:543–560, 1987.
- 7 E. M. Shoemaker and R. F. Wolfe. Cratering time scales for the Galilean
8 satellites. In D. Morrison, editor, *Satellites of Jupiter*, pages 277–339, 1982.
- 9 E. M. Shoemaker, R. F. Wolfe, and C. S. Shoemaker. Asteroid and comet flux
10 in the neighborhood of Earth. In V. Sharpton and P. Ward, editors, *Global
11 catastrophes in Earth history*, pages 155–170. Geol. Soc. Am. special paper
12 247, Boulder, 1990.
- 13 L. A. Soderblom and L. Lebofsky. Technique for rapid determination of rel-
14 ative ages of lunar areas from orbital photography. *J. Geophys. Res.*, 77:
15 279–296, 1972.
- 16 C. P. Sonett and M. A. Chan. Neoproterozoic Earth-Moon dynamics: Rework
17 of the 900 Ma Big Cottonwood Canyon tidal laminae. *Geophys. Res. Lett.*
18 , 25:539–542, 1998.
- 19 S. T. Stewart and G. J. Valiant. Martian subsurface properties and crater for-
20 mation processes inferred from fresh impact crater geometries. *Meteoritics
21 and Planetary Science*, 41:1509–1537, 2006.
- 22 D. Stöffler and G. Ryder. Stratigraphy and isotope ages of lunar geologic
23 units: Chronological standard for the inner Solar System. *Space Sci. Rev.*,
24 96:9–54, 2001.
- 25 R. G. Strom and G. Neukum. The cratering record on mercury and the origin
26 of impacting objects. In *Mercury*, pages 336–373. University of Arizona

- 1 Press, Tucson, 1988.
- 2 R. G. Strom, G. G. Schaber, and D. D. Dawsow. The global resurfacing of
3 Venus. *J. Geophys. Res.*, 99:10899–10926, 1994.
- 4 R. G. Strom, R. Malhotra, T. Ito, F. Yoshida, and D. A. Kring. The origin
5 of planetary impactors in the inner solar system. *Science*, 309:1847–1850,
6 2005.
- 7 J. S. Stuart. A Near-Earth Asteroid population estimate from the LINEAR
8 survey. *Science*, 294:1691–1693, 2001.
- 9 J. S. Stuart. Observational constraints on the number, albedos, sizes, and
10 impact hazards of the near-Earth asteroids. *PhD thesis. Massachusetts*
11 *Institute of Technology, Cambridge, MA.*, 2003.
- 12 J. S. Stuart and R. P. Binzel. Bias-corrected population, size distribution, and
13 impact hazard for the near-Earth objects. *Icarus*, 170:295–311, 2004.
- 14 T. D. Swindle, P. D. Spudis, G. J. Taylor, R. L. Korotev, and R. H. Nichols, Jr.
15 Searching for crism basin ejecta - chemistry and ages of luna 20 impact
16 melts. *Proceedings of the 21th Lunar and Planetary Science Conference*,
17 pages 167–181, 1991, abstract no 1229.
- 18 F. Tera, D. A. Papanastassiou, and G. J. Wasserburg. Isotopic evidence for a
19 terminal lunar cataclysm. *Earth and Planetary Science Letters*, 22(1), 1974.
- 20 T. W. Thompson, W. J. Roberts, W. K. Hartmann, R. W. Shorthill, and S. H.
21 Zisk. Blocky craters: Implications about the lunar megaregolith. *Moon and*
22 *Planets*, 21:319–342, 1979.
- 23 N. Warren and R. Trice. Structure in the upper lunar crust. *Roy. Soc. of*
24 *London Phil. Trans. Series A*, 285:469–473, 1977.
- 25 S. C. Werner, A. W. Harris, G. Neukum, and B. A. Ivanov. NOTE: The
26 Near-Earth Asteroid Size-Frequency Distribution: A Snapshot of the Lunar

- 1 Impactor Size-Frequency Distribution. *Icarus*, 156:287–290, 2002.
- 2 P. Wessel and W. H. F. Smith. Free software helps map and display data.
- 3 *EOS Transactions*, 72:441–441, 1991.
- 4 G. W. Wetherill. Collisions in the asteroid belt. *J. Geophys. Res.*, 72:2429–
- 5 2444, 1967.
- 6 M. A. Wieczorek and M. Le Feuvre. Did a large impact reorient the moon?
- 7 *Icarus*, 200:358–366, 2009.
- 8 W. Wiesel. The meteorite flux at the lunar surface. *Icarus*, 15:373–383, 1971.
- 9 D. E. Wilhelms, J. F. McCauley, and N. J. Trask. *The geologic history of the*
- 10 *Moon*. Washington: U.S. G.P.O. ; Denver, U.S. Geological Survey, 1987.
- 11 J. A. Wood. Bombardment as a cause of the lunar asymmetry. *Moon*, 8:
- 12 73–103, 1973.
- 13 K. Zahnle, L. Dones, and H. F. Levison. Cratering rates on the Galilean
- 14 satellites. *Icarus*, 136:202–222, 1998.
- 15 K. Zahnle, P. Schenk, S. Sobieszczyk, L. Dones, and H. F. Levison. Differential
- 16 cratering of synchronously rotating satellites by ecliptic comets. *Icarus*, 153:
- 17 111–129, 2001.

1 List of Figures

2	1	Impactor SFD	71
3	2	Model production function of lunar craters	72
4	3	Planetary cratering rates relative to the Moon	73
5	4	Probability distribution of impact velocities	74
6	5	Lunar asymmetries	75
7	6	Model vs. rayed crater Apex/Antapex distribution	76
8	7	Apex/Antapex effect vs. previous work	77
9	8	Crater chronology curve	78
10	9	Age estimates	79

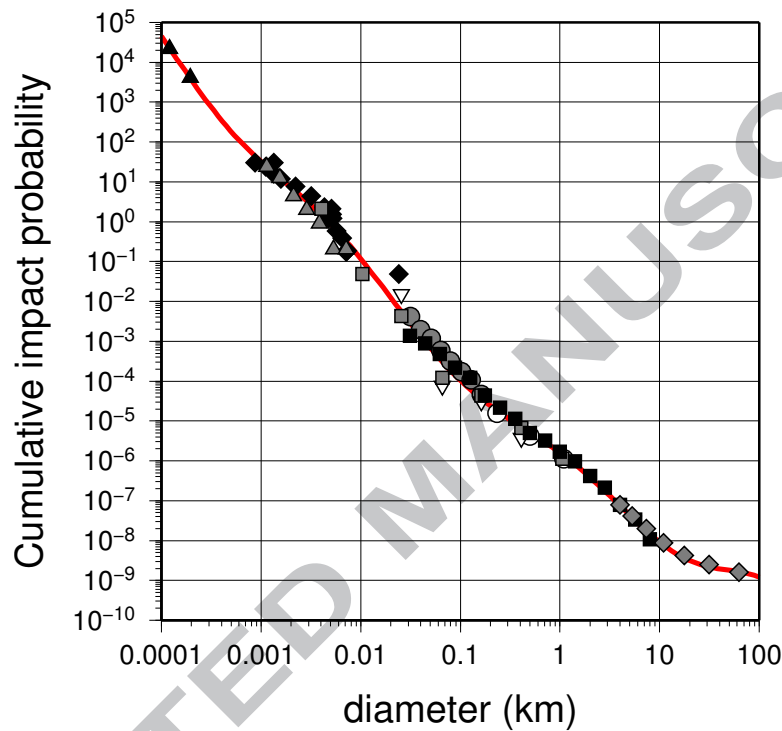


Fig. 1. Impact probability per year on Earth, for impactors larger than a given diameter. Estimates come from atmospheric records or Öpik probabilities derived from telescopic observations (*black triangles*: Halliday et al. (1996); *black diamonds*: ReVelle (2001); *grey triangles*: Brown et al. (2002); *grey squares and white triangles*: Rabinowitz et al. (2000); *grey circles*: Harris, A. W. (2002); *white circles*: Morbidelli et al. (2002); *black squares*: Stuart and Binzel (2004)). Our compilation at large sizes is augmented by including the observed size-frequency distribution of Mars-crossing objects with sizes greater than 4 km, scaled to the terrestrial impact rates of Stuart and Binzel (2004) (*grey diamonds*). The red curve is the best fit polynomial.

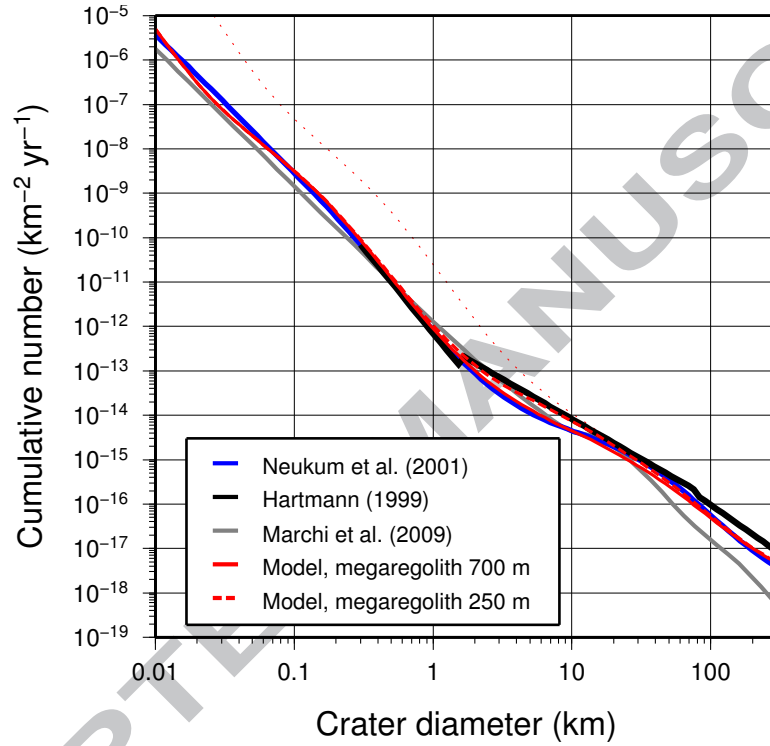


Fig. 2. Model production function of lunar craters, for one year, in comparison with the Hartmann and Neukum measured production functions, and the model production function of Marchi et al. (2009). Respective megaregolith thicknesses of 700 and 250 m allow to fit either the Neukum or Hartmann production functions in the diameter range 2–20 km. The thin dotted red curve is obtained by using only the non-porous scaling relation.

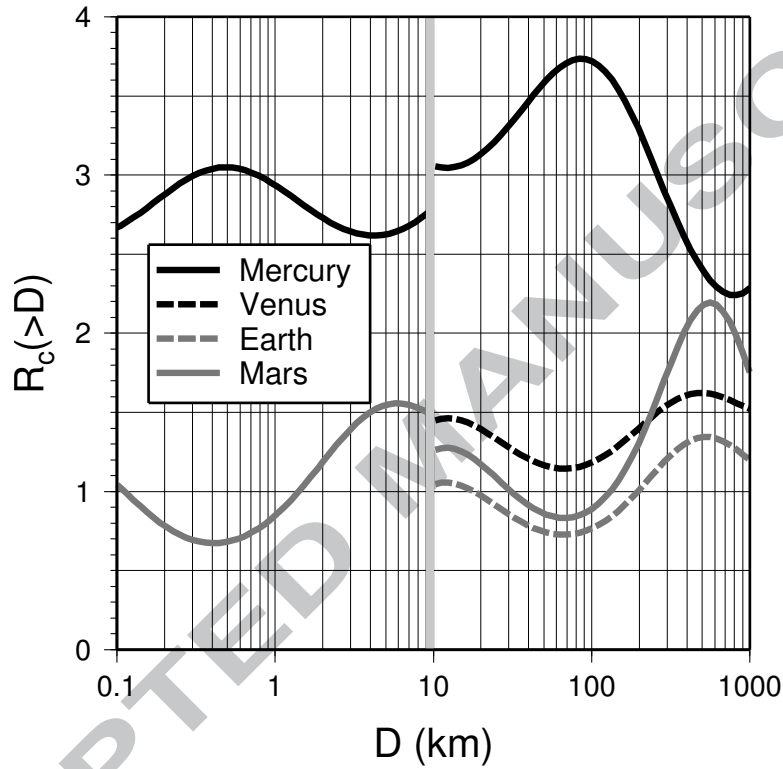


Fig. 3. Planetary cratering ratios with respect to the Moon, for craters larger than a given diameter D . For illustrative purposes, craters with $D < 10$ km and $D > 10$ km are respectively assumed to form in the porous and non-porous regimes. Curves are not shown for Venus and the Earth for $D < 10$ km, since the porous regime is not expected, and erosion or atmospheric shielding are known to be of significant influence at these sizes.

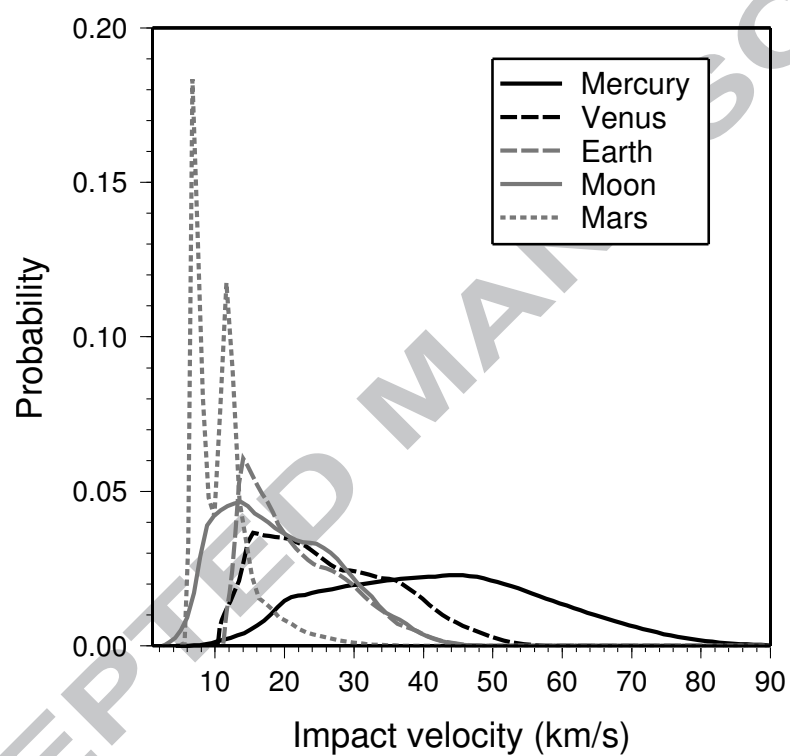


Fig. 4. Probability distribution of impact velocities for the Moon and terrestrial planets.

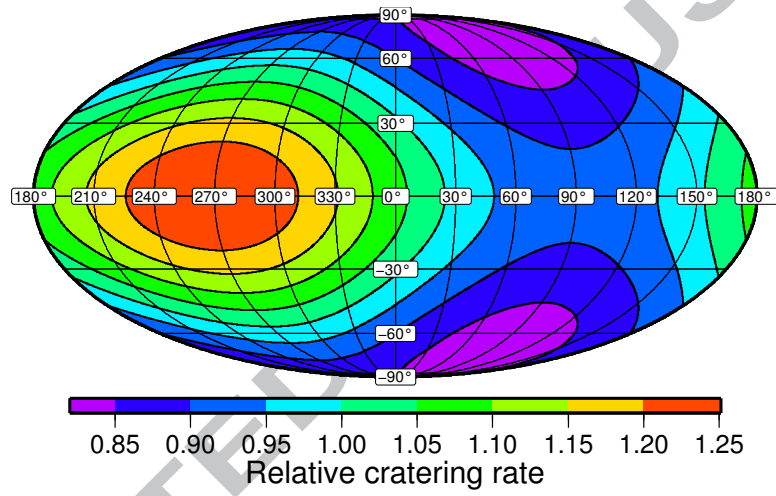


Fig. 5. Relative cratering rate on the Moon for the current Earth-Moon distance and for crater diameters larger than 1 km. This image is plotted in a Mollweide projection centered on the sub-Earth point.

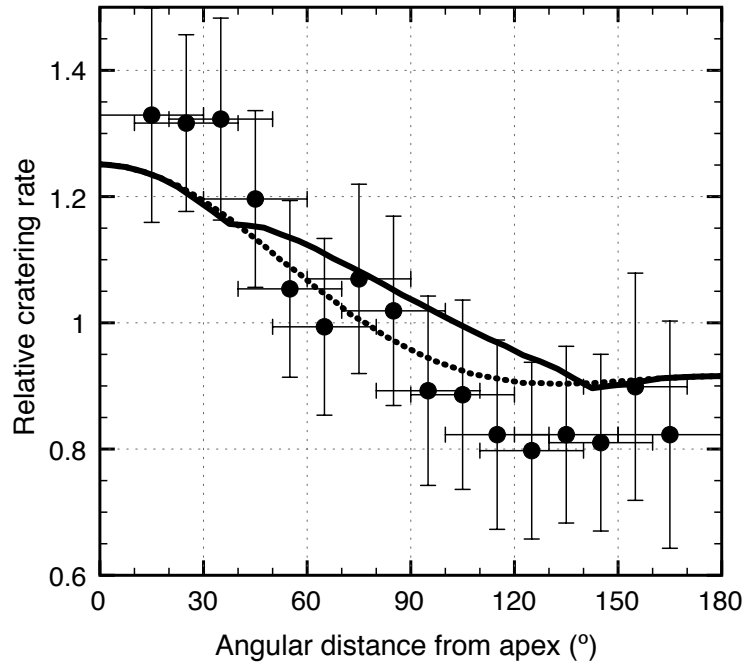


Fig. 6. Relative lunar cratering rate as a function of angular distance from the apex of motion. Rayed crater data are for crater diameters greater than 5 km from Morota et al. (2005) that were counted between approximately $[70^{\circ}\text{E}, 290^{\circ}\text{E}]$ in longitude and $[-42^{\circ}\text{N}, 42^{\circ}\text{N}]$ in latitude. In comparison, the predicted apex/antapex cratering effect is shown over the same count area (solid black) and for the entire Moon (dotted black).

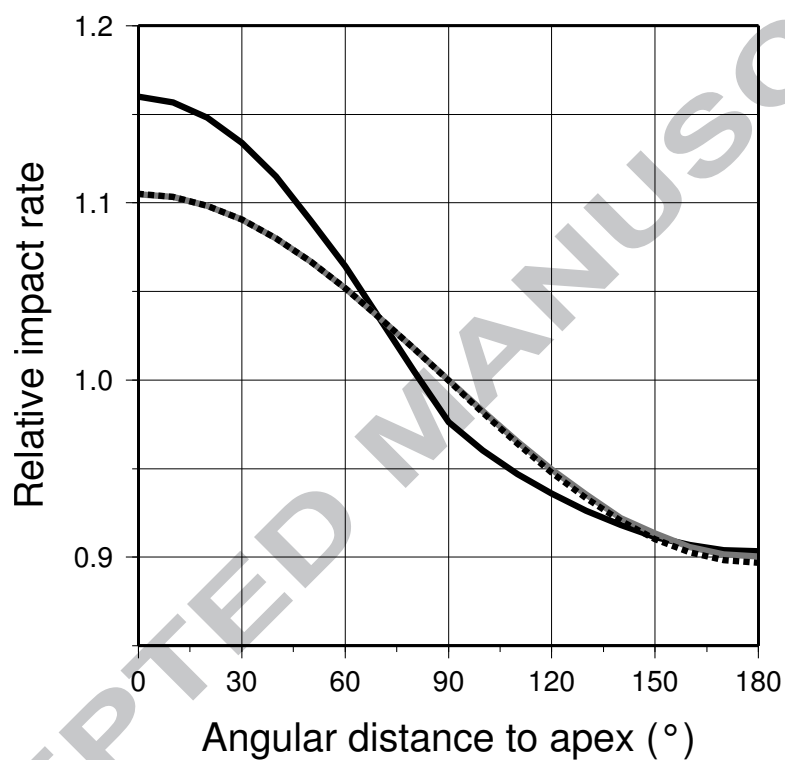


Fig. 7. Relative lunar impact rate as a function of the angular distance from the apex (solid black), in comparison with the equation from Zahnle et al. (2001) (solid grey). The latter is reproduced if the model forces latitudinal isotropy of encounter inclinations (dotted black).

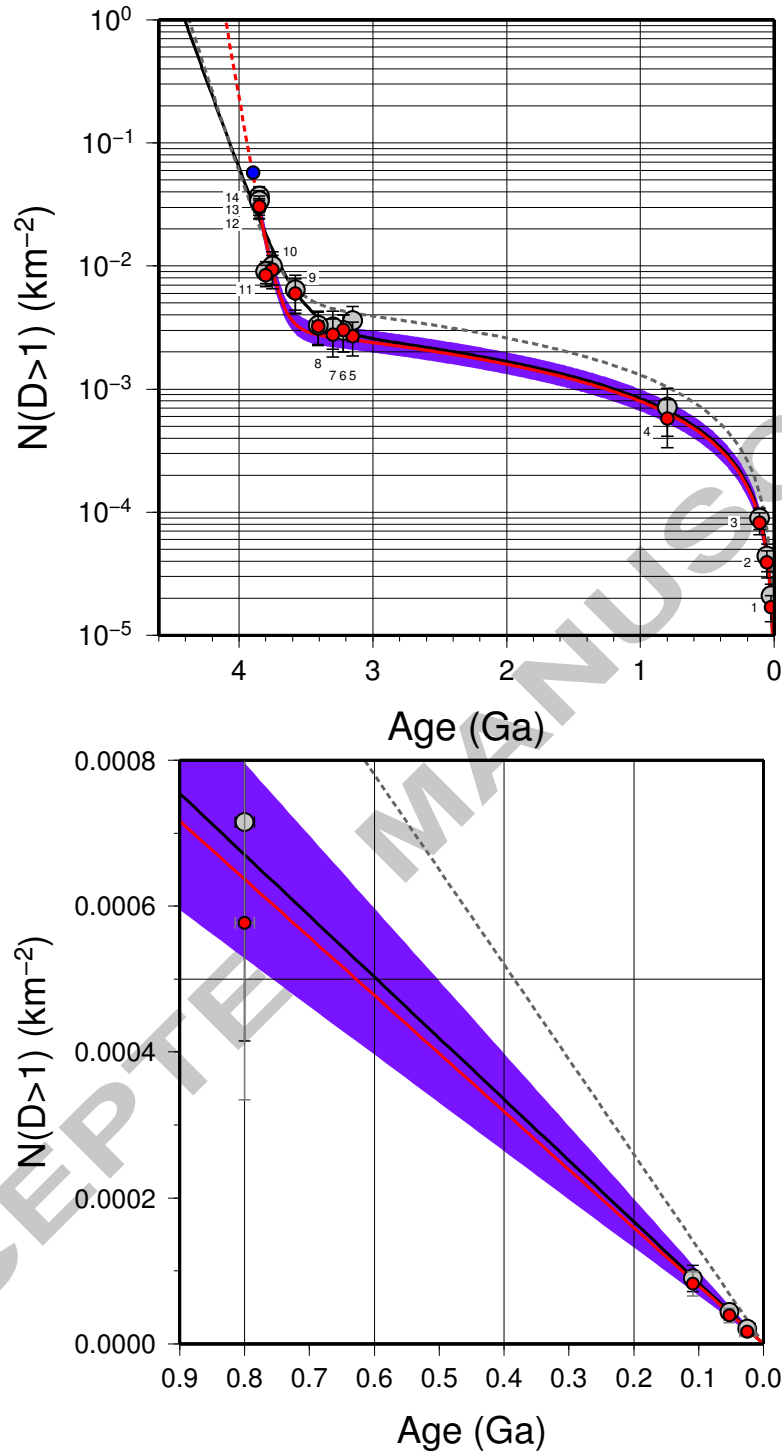


Fig. 8. Lunar crater chronology calibration curve. Calibration points, listed in table 9, are shown before (*grey circles*) and after (*red circles*) accounting for the spatially-dependent cratering rate. Our proposed analytic fit (*red line*) is compared to the curves of Neukum et al. (2001a) (*solid black*) and Marchi et al. (2009) (*dashed grey*). Crisium basin, that was not included in the fit, is shown in blue. Also shown is the range of bias in age that could be produced by spatial variations in the cratering rate (*purple area*).

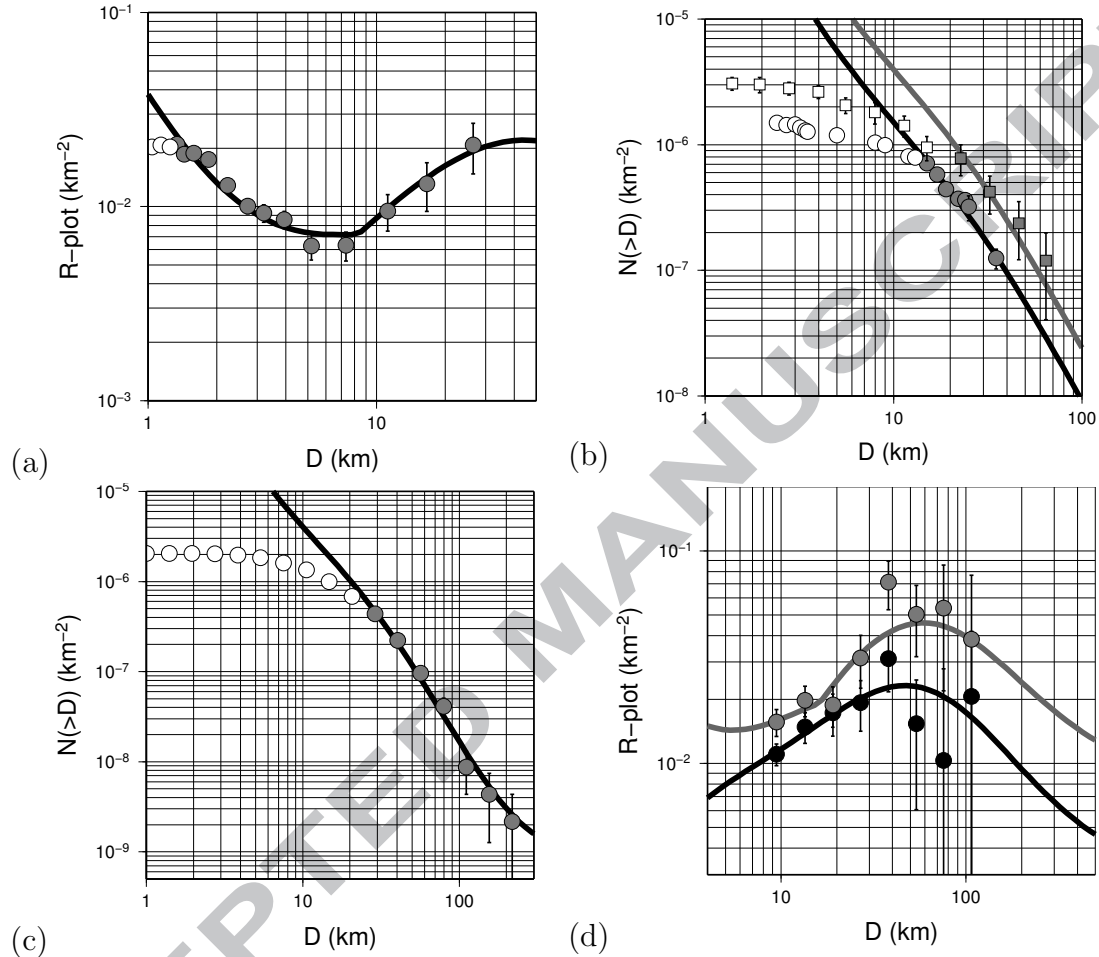


Fig. 9. Age estimates. Distributions plotted either in cumulative form or R-plot. Data represented by white circles are not included in the fit, either because of saturation (Moon), erosion (Earth) or atmospheric shielding (Venus). (a) Orientale basin: 3.73 ± 0.01 Ga with a megaregolith thickness of 500 m. Data from Neukum et al. (2001a) (b) Terrestrial cratering record: 138 ± 6 Ma for the estimates of Hughes (2000) (circles), 390 ± 75 Ma for the Phanerozoic cratons investigated by Grieve and Dence (1979) (squares) (c) Venusian surface: 240 ± 13 Ma. Data from the Magellan mission (d) Caloris basin lineated sculpture (grey): 3.73 ± 0.2 Ga with a megaregolith thickness of 900 m; Caloris interior plains (black): 3.30 ± 0.3 Ga with a megaregolith thickness of 250 m. Data from Fassett et al. (2009).

1 List of Tables

2	1	Impactor SFD coefficients	81
3	2	Crater SFDs coefficients	82
4	3	Impact conditions with respect to the Moon	83
5	4	Unnormalized associated Legendre functions	84
6	5	Lunar impact asymmetry coefficients	85
7	6	Lunar crater asymmetry coefficients	86
8	7	Planetary impact asymmetry coefficients	87
9	8	Planetary crater asymmetry coefficients	88
10	9	Corrected calibration points of the crater chronology	89

Table 1

Impactor size distribution: $\log s(> d) = \sum_{i=0}^{10} s_i (\log d_{\text{km}})^i$.

s_0	s_1	s_2	s_3	s_4	s_5
1.0	3.1656E-01	1.0393E-01	5.7091E-02	-8.1475E-02	-2.9864E-02
s_6	s_7	s_8	s_9	s_{10}	
1.3977E-02	5.8676E-03	-4.6476E-04	-3.8428E-04	-3.7825E-05	

Table 2

Planetary crater size-frequency distributions for 1 year (km^{-2}): $\log \bar{C}(> D) = \sum_{i=0}^{10} C_i (\log D_{\text{km}})^i$, $D \in [0.1 - 1000]$ km.

	Moon non-porous	Moon porous	Mercury non-porous	Mercury porous	Venus non-porous
C_0	-0.1049E+02	-0.1206E+02	-0.9939E+01	-0.1159E+02	-0.1073E+02
C_1	-0.4106E+01	-0.3578E+01	-0.3994E+01	-0.3673E+01	-0.4024E+01
C_2	-0.8715E+00	0.9917E+00	-0.1116E+01	0.9002E+00	-0.4503E-01
C_3	0.1440E+01	0.7884E+00	0.1269E+01	0.9609E+00	0.1374E+01
C_4	0.1000E+01	-0.5988E+00	0.1272E+01	-0.5239E+00	0.2433E+00
C_5	-0.8733E+00	-0.2805E+00	-0.8276E+00	-0.3622E+00	-0.7040E+00
C_6	-0.2725E+00	0.1665E+00	-0.3718E+00	0.1508E+00	-0.3962E-01
C_7	0.2373E+00	0.3732E-01	0.2463E+00	0.5224E-01	0.1541E+00
C_8	0.9500E-02	-0.1880E-01	0.2091E-01	-0.1843E-01	-0.8944E-02
C_9	-0.2438E-01	-0.1529E-02	-0.2756E-01	-0.2510E-02	-0.1289E-01
C_{10}	0.3430E-02	0.7058E-03	0.3659E-02	0.8053E-03	0.2102E-02
	Earth non-porous	Mars (long term) non-porous	Mars (long term) porous	Mars (today) non-porous	Mars (today) porous
C_0	-0.1099E+02	-0.1089E+02	-0.1213E+02	-0.1082E+02	-0.1207E+02
C_1	-0.3996E+01	-0.4068E+01	-0.3124E+01	-0.4072E+01	-0.3134E+01
C_2	0.2334E+00	0.2279E+00	0.1295E+01	0.2157E+00	0.1293E+01
C_3	0.1333E+01	0.1422E+01	0.1542E+00	0.1426E+01	0.1713E+00
C_4	0.2286E-02	0.2470E-01	-0.7519E+00	0.3330E-01	-0.7518E+00
C_5	-0.6476E+00	-0.7150E+00	0.3125E-01	-0.7171E+00	0.2232E-01
C_6	0.2875E-01	0.2056E-01	0.1779E+00	0.1856E-01	0.1786E+00
C_7	0.1313E+00	0.1535E+00	-0.2311E-01	0.1540E+00	-0.2129E-01
C_8	-0.1410E-01	-0.1526E-01	-0.1369E-01	-0.1510E-01	-0.1396E-01
C_9	-0.1006E-01	-0.1252E-01	0.2623E-02	-0.1255E-01	0.2492E-02
C_{10}	0.1810E-02	0.2247E-02	0.5521E-05	0.2246E-02	0.3212E-04

Table 3

Impact rate, mean impact velocity and surface gravity for the inner planets, normalized to the Moon's.

	Moon	Mercury	Venus	Earth	Mars (long term)	Mars (today)
impact rate ratio	1	1.82	1.75	1.58	2.76	3.20
mean velocity ratio	1	2.16	1.28	1.04	0.53	0.54
surface gravity ratio	1	2.2	5.3	5.9	2.2	2.2

Table 4
Unnormalized associated Legendre functions

l, m	$P_{lm}(\sin \lambda)$
0, 0	1
1, 1	$\cos \lambda$
2, 0	$\frac{1}{2}(3 \sin^2 \lambda - 1)$
2, 2	$3 \cos^2 \lambda$
3, 1	$\frac{3}{2}(5 \sin^2 \lambda - 1) \cos \lambda$
4, 0	$\frac{1}{8}(35 \sin^4 \lambda - 30 \sin^2 \lambda + 3)$

Table 5

Spherical harmonic coefficients of the lunar relative impact flux $\Delta\phi(\lambda, \varphi)$ for Earth–Moon separations of 30, 45, and 60 Earth radii.

C_{lm}	30 Earth radii	45 Earth radii	60 Earth radii
$C_{0,0}$	1	1	1
$C_{1,-1}$	$-1.7779020 \times 10^{-1}$	$-1.4591830 \times 10^{-1}$	$-1.2670400 \times 10^{-1}$
$C_{2,0}$	$-6.3209891 \times 10^{-2}$	$-6.2923420 \times 10^{-2}$	$-6.2755592 \times 10^{-2}$
$C_{2,2}$	$-1.7937283 \times 10^{-3}$	$-1.2524090 \times 10^{-3}$	$-9.8998262 \times 10^{-4}$
$C_{4,0}$	$-9.9735381 \times 10^{-3}$	$-1.0141450 \times 10^{-2}$	$-1.0222370 \times 10^{-2}$

Table 6

Spherical harmonic coefficients of the lunar relative cratering rate $\Delta C(D > 1, \lambda, \varphi)$ for Earth–Moon separations of 30, 45, and 60 Earth radii.

C_{lm}	30 Earth radii	45 Earth radii	60 Earth radii
$C_{0,0}$	1	1	1
$C_{1,-1}$	$-2.2715950 \times 10^{-1}$	$-1.8571530 \times 10^{-1}$	$-1.6092760 \times 10^{-1}$
$C_{2,0}$	$-1.3954110 \times 10^{-1}$	$-1.3874170 \times 10^{-1}$	$-1.3831914 \times 10^{-1}$
$C_{2,2}$	$-3.3499412 \times 10^{-3}$	$-2.2729362 \times 10^{-3}$	$-1.7822560 \times 10^{-3}$
$C_{3,-1}$	2.9040180×10^{-3}	2.3263713×10^{-3}	1.9948010×10^{-3}
$C_{4,0}$	2.7412530×10^{-3}	2.7863080×10^{-3}	2.8083000×10^{-3}

Table 7

Spherical harmonic coefficients of the relative impact flux $\Delta\phi(\lambda)$ for the terrestrial planets.

Planet	C_{00}	C_{20}	C_{40}
Mercury	1	3.7395410×10^{-2}	$-7.9170623 \times 10^{-3}$
Venus	1	7.3546990×10^{-3}	$-6.0267052 \times 10^{-3}$
Earth	1	$-2.6165971 \times 10^{-2}$	$-1.8682412 \times 10^{-3}$
Mars (today)	1	1.6254980×10^{-1}	$-1.0738801 \times 10^{-2}$
Mars (long-term average)	1	8.7425552×10^{-2}	4.7442493×10^{-3}

Table 8

Spherical harmonic coefficients of the relative cratering rate $\Delta C(D > 1, \lambda)$ for the terrestrial planets.

Planet	C_{00}	C_{20}	C_{40}
Mercury	1	4.5850560×10^{-2}	2.4749320×10^{-3}
Venus	1	$-1.8545722 \times 10^{-3}$	3.5865970×10^{-4}
Earth	1	$-7.6586370 \times 10^{-2}$	2.4353234×10^{-4}
Mars (today)	1	3.3900970×10^{-1}	2.2655340×10^{-3}
Mars (long-term average)	1	1.7986312×10^{-1}	$-4.3484250 \times 10^{-4}$

Table 9

Lunar crater chronology calibration points used in this study, and their spatial correction.

Geologic unit	Location	Age (Ga)	Measured crater density (10^{-4} km^{-2})	Globally averaged crater density (10^{-4} km^{-2})
1 Cone crater	-3.7°N, -17.5°E	0.025	0.21	0.169
2 North Ray crater	-9°N, -15.6°E	0.053	0.44	0.390
3 Tycho crater	-43.4°N, -11.1°E	0.109	0.90	0.824
4 Copernicus	9.7°N, -20.1°E	0.80	7.15	5.77
5 Ocean Procellarum (A12)	18.4°N, -57.4°E	3.15	36	29.7
6 Mare Crisium (L24)	17.0°N, 59.1°E	3.22	30	30.2
7 Mare Imbrium (A15)	32.8°N, -15.6°E	3.30	32	27.7
8 Mare Fecunditatis (L16)	-7.8°N, 51.3°E	3.41	33	32.4
9 Mare Tranquilitatis (young) (A11)	8.5°N, 31.4°E	3.58	64	60.1
10 Mare Serenitatis (A17)	28.0°N, 17.5°E	3.75	100	93.6
11 Mare Tranquilitatis (old) (A11)	8.5°N, 31.4°E	3.80	90	84.5
12 Imbrium/Apennines	18.9°N, -3.7°E	3.85	350	301
13 Fra Mauro (A14)	-3.7°N, -17.5°E	3.85	370	298
14 Descartes (A16)	-9.0°N, 15.6°E	3.85	340	306